Final Scientific/Technical Report

Submitted to: Department of Energy – National Energy Technology Laboratory

Experimental Demonstration of Alkalinity Concentration Swing for Direct Air Capture of CO₂

Award No. DE-FE0031964

SUBMITTED BY

PRINCIPAL INVESTIGATOR: Daniel P. Schrag

Co-Investigator: Michael Aziz

Graduate student researchers: Andrew Bergman, Anatoly Rinberg

(617) 495-7676

daniel_schrag@harvard.edu

Submission Date: 12/21/2023

DUNS Number: 0823596910000

Recipient Organization: Harvard University, 26 Oxford Street, 4th Floor, Cambridge, MA 02138

Project Period: 2/9/2021 to 8/8/2023

Signature:

Daniel Schrag

Executive Summary:

This work constitutes the first lab-scale experimental demonstration of the alkalinity concentration swing (ACS) for direct air capture (DAC) of CO_2. ACS can be implemented by taking a dilute alkaline solution that has contacted ambient air, and then concentrating it using commercially available desalination technologies. The more concentrated solution has a higher partial pressure of CO_2 relative to the initial solution, allowing the CO_2 to be separated and stored. The ACS approach is based on simple thermodynamics but had never been verified experimentally in terms of extracting CO_2 from air until now. We tested two distinct methods for concentrating the alkaline liquid: reverse osmosis (RO) and capacitive deionization (CDI). We found that to complete the DAC cycle in feasible operating conditions, a bicarbonate-enrichment step needed to be introduced, which selects on bicarbonate ions over carbonate ions. Two approaches for CO_2 extraction to measure the CO_2 yield per amount of water processed by the ACS method were tested. The energy required per amount of CO_2 captured was quantified. We further applied an energy model to study how operating the ACS cycle under different conditions would affect energy requirements.

PROJECT TITLE: EXPERIMENTAL DEMONSTRATION OF ALKALINITY CONCENTRATION SWING FOR DIRECT AIR CAPTURE OF CARBON DIOXIDE

ANATOLY RINBERG,[*†] **ANDREW M. BERGMAN,**[*†] **MICHAEL J. AZIZ,**[†] **DANIEL P. SCHRAG**[§†]

[†]John A. Paulson School of Engineering and Applied Sciences
Harvard University
Cambridge, Massachusetts, 02138, USA

[§]Dept. of Earth and Planetary Sciences
Harvard University
Cambridge, Massachusetts, 02138, USA

ABSTRACT

This work constitutes the first lab-scale experimental demonstration of the alkalinity concentration swing (ACS) for direct air capture (DAC) of CO_2. ACS can be implemented by taking a dilute alkaline solution that has contacted ambient air, and then concentrating it using commercially available desalination technologies. The more concentrated solution has a higher partial pressure of CO_2 relative to the initial solution, allowing the CO_2 to be separated and stored. The ACS approach is based on simple thermodynamics but had never been verified experimentally in terms of extracting CO_2 from air until now. We tested two distinct methods for concentrating the alkaline liquid: reverse osmosis (RO) and capacitive deionization (CDI). We found that to complete the DAC cycle in feasible operating conditions, a bicarbonate-enrichment step needed to be introduced, which selects on bicarbonate ions over carbonate ions. Two approaches for CO_2 extraction to measure the CO_2 yield per amount of water processed by the ACS method were tested. The energy required per amount of CO_2 captured was quantified. We further applied an energy model to study how operating the ACS cycle under different conditions would affect energy requirements.

Contents

1   Introduction

Reducing greenhouse gas emissions as much and as fast as possible must be prioritized to avoid the worst harms from climate change, which will be felt most by vulnerable populations and frontline communities.[1] However, beyond emission reductions, in its Sixth Assessment Report, the Intergovernmental Panel on Climate Change states that the "deployment of carbon dioxide removal to counterbalance hard-to-abate residual emissions is unavoidable if net zero CO_2 or [greenhouse gas] emissions are to be achieved."[2] Therefore, for global warming to be halted this century, gigatonne scale CDR will need to be deployed,[3] especially to offset emissions from agriculture and long-haul aviation. However, aiming for extremely large CDR deployment, such as 10 to 20 billion tonnes of removal annually by mid to late century, brings along significant moral hazard. The many reports and policy proposals advocating for these large scales pose the risk of reducing the political incentive to reduce emissions in the short term.[4,5]

Direct air capture (DAC) coupled with carbon storage has been proposed as one of many approaches to implement carbon dioxide removal. In this work, we conducted experimental verification of a new DAC approach, the alkalinity concentration swing (ACS; described in Section 2). ACS is implemented by taking a dilute alkaline solution that has approached equilibrium with air and then concentrating it using commercially available desalination technologies. The more concentrated solution has a higher partial pressure of CO_2 relative to the initial solution, allowing the CO_2 to be separated and stored. The ACS approach is based on simple thermodynamics, but this is the first work to experimentally verify or to quantify its ability to capture CO_2 from air.

We first developed an accurate Aqueous DIC Model to measure the alkalinity and carbon concentration in solution (Section 3). Two approaches for CO_2 extraction were developed to measure the CO_2 yield per amount of water processed by the ACS (Section 4). Re-equilibration was demonstrated by exposing the diluted post-extraction solution to gas mixtures matching atmospheric conditions (Section 5). We then tested, in parallel, two distinct methods for concentrating the alkaline liquid: reverse osmosis (RO; Section 6) and capacitive deionization (CDI; Section 7). RO and CDI methods were studied extensively across a range of operating conditions, and their ability to concentrate alkalinity was characterized.

Through this work, shortcomings of the ACS were identified and a modification was introduced to demonstrate a feasible DAC cycle. After CO_2 absorption, introducing a bicarbonate-enrichment step, which selects bicarbonate ions over carbonate ions, significantly increases the performance of the ACS cycle (8). This modified cycle is called the bicarbonate-enriched alkalinity concentration swing (BE-ACS), and is discussed in detail in Section 8. We further demonstrate that CDI is able to be used to perform this bicarbonate-enrichment step. Finally, integrating the bicarbonate-enriched ACS process, the energy required per amount of CO_2 captured was quantified (Section 9). We then applied an energy model, developed in our previous work,[6] to study how operating the ACS cycle under different conditions would affect energy requirements.

2   Background for the alkalinity concentration swing

The foundational basis for the ACS was first introduced and published in a theoretical study: Anatoly Rinberg*, Andrew M. Bergman*, Daniel P. Schrag, and Michael J. Aziz. "Alkalinity Concentration Swing for Direct Air Capture of Carbon Dioxide." ChemSusChem 14, no. 20 (2021): 4439–53. https://doi.org/10.1002/cssc.202100786 (*authors contributed equally to this work).[6]

The ACS is based on the fact that an alkaline aqueous solution that has been loaded with dissolved inorganic carbon (DIC) — the sum of carbonate ion (CO_3^{-2}), bicarbonate ion (HCO_3^-), and dissolved aqueous carbon dioxide ($CO_2(aq)$) concentrations in solution — increases its partial pressure of CO_2 when that solution is concentrated, e.g. by

removing water. Applying a vacuum to the concentrated solution causes CO_2 to outgas. After outgassing, if the same alkaline aqueous solution is diluted, CO_2 is absorbed from the air and the DIC concentration increases.

The four steps of the ACS are schematically portrayed in Figure 1A. Feed solution is first concentrated (Step $1 \rightarrow 2$) through the concentrating alkalinity module. Concentrated solution is then sent to the outgassing module (Step $2 \rightarrow 3$). The dilute stream and the post-outgassing solution stream is recombined and alkalinity is diluted (Step $3 \rightarrow 4$). Finally, CO_2 is re-absorbed through a contacting module (Step $4 \rightarrow 1$).
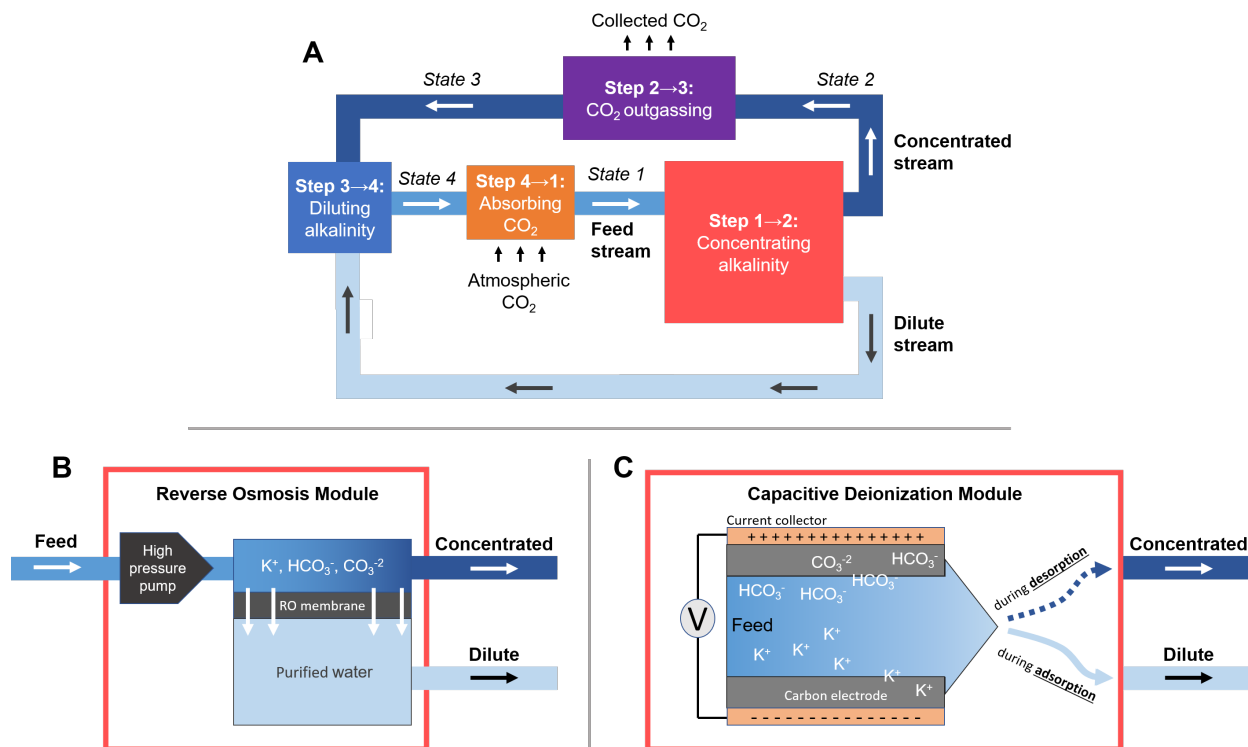
Figure 1: **ACS system schematic.** (A) The four steps of the ACS represented in a full cycle. (B) A schematic of a reverse osmosis module driven by a high-pressure pump. (C) A schematic of a capacitive deionization module driven by applied current and voltage. Ion exchange membranes are not represented in the diagram.

The ACS cycle can also be represented on a DIC-to-alkalinity diagram that plots the iso-pCO_2 lines as a function of the DIC-to-alkanity ratio and alkalinity concentration (Figure 2). On such a diagram, moving right and left on the plot, at a fixed DIC-to-alkalinity ratio, is equivalent to an ideal process of concentration and dilution, respectively. This diagram demonstrates that the DIC-to-alkalinity ratio increases during the absorption step, but must stay below the 0.4 mbar iso-pCO_2 line. Concentrating the solution crosses increasing iso-pCO_2 lines, thereby allowing for CO_2 extraction upon vacuum application. We chose 50 mbar vacuum for the outgassing CO_2 partial pressure as a reasonable but un-optimized parameter that is relatively low, but is above the water vapor pressure of 23 mbar at 20 °C.

3   Testing and calibration of CO_2 analysis system

We developed an Aqueous Dissolved Inorganic Carbon Model (ADICM), based on an empirically-generated aqueous chemistry model (PHREEQC Version 3). To generate alkalinity-to-DIC diagrams and computationally study ACS conditions, ADICM was used to calculate solution conditions for fixed pH, fixed partial pressure, and fixed DIC. We also used ADICM to create an inverse function that outputs the alkalinity and DIC concentrations based on the measured pH, conductivity, and temperature of a given sample. The model implements Pitzer equations to accurately calculate
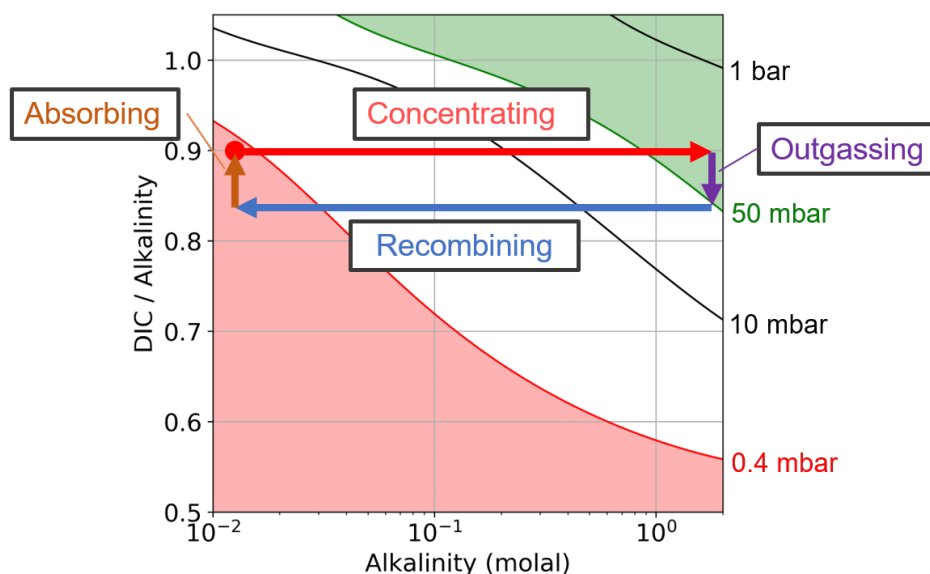
Figure 2: **ACS DIC-to-alkalinity diagram.** DIC-to-alkalinity diagram with arrows schematically representing the four steps of the ACS cycle. Curves represent iso-p_{CO_2} lines. A DIC-to-alkalinity ratio of 1 corresponds to regime where DIC ions are bicarbonate, and a ratio of 0.5 corresponds to all carbonate ions. The shaded red area is the parameter space corresponding to partial pressure below 0.4 mbar. The shaded green area is parameter space corresponding to partial pressure above 50 mbar.

activity coefficient databases as ionic strength, temperature, and ion species are varied.[7] The model is based on activity coefficients for a wide range of ion species and their interactions, and can be applied to high-salinity waters that are beyond the range of application for the Debye-Hückel theory.
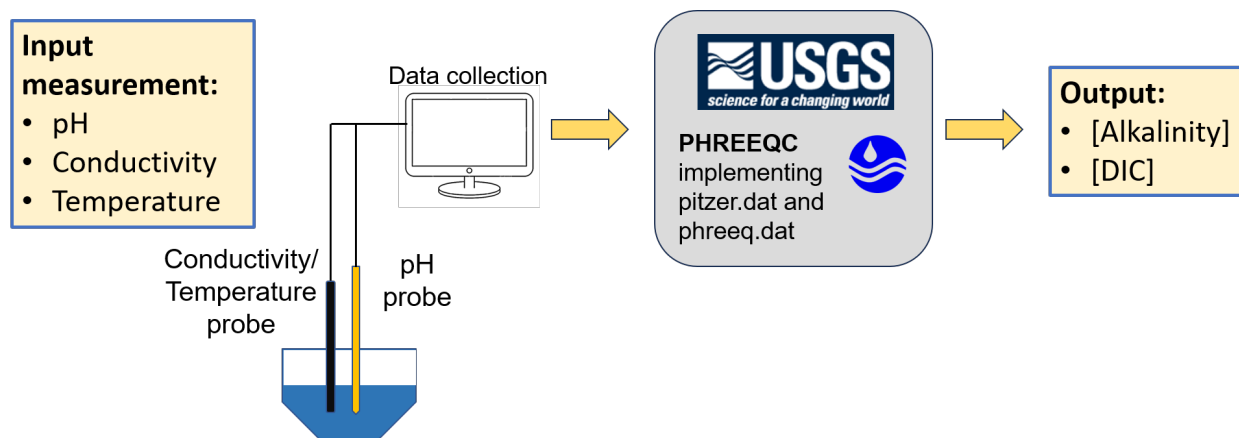
Figure 3: **PHREEQC Inverse Function Protocol.** The inverse function protocol relies on the Aqueous DIC Model, which implements PHREEQC Version 3 (`https://www.usgs.gov/software/phreeqc-version-3`).

Using the ADICM, we developed an inverse function to translate a measurement of conductivity, pH, and temperature to the alkalinity and DIC concentrations (Fig. 3). To validate our method and bound the uncertainty on our measurement, we prepared 30 solutions with a sodium cation (from 20 to 800 mM) and different fraction of DIC-to-alkalinity, 50-100% (Fig. 4). For example, at 50 mM Na$^+$ we produced 5 solutions with 25, 31.25, 37.5, 43.75, and 50 mM DIC. We found that below 150 mM alkalinity, the model matched the data to within 5% error.

In addition to the implemented aqueous geochemical model (PHREEQC) and the pH and conductivity testing protocol, the Dissolved Inorganic Carbon (DIC) Analyzer (purchased from Apollo Scitech LLC) was calibrated.

6
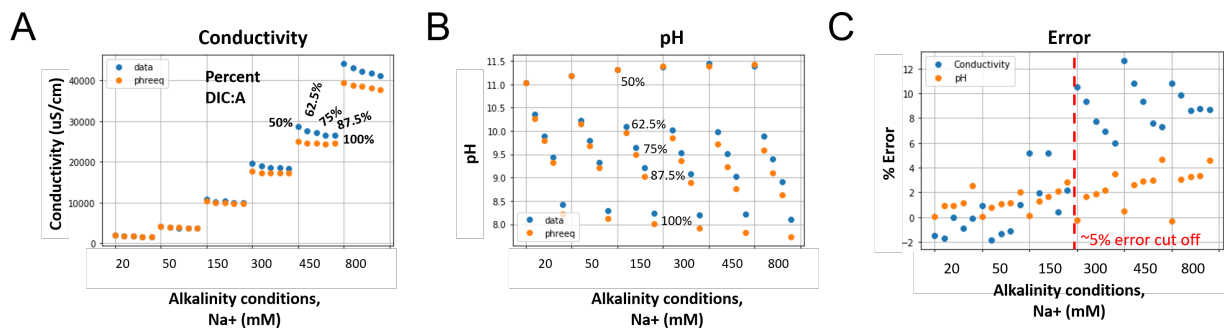
Figure 4: **PHREEQC Inverse Function Error Analysis.** (A-B) Blue points are measured conductivity and pH data from prepared solutions; orange points are equivalent conditions modeled using PHREEQ. (C) % error is plotted for pH (orange) and conductivity (blue) for all the different conditions. The 5% error cut-off is noted as a red dashed line.

Because the DIC Analyzer operates optimally for lower DIC concentrations ($\sim$2-20 mM), a protocol for diluting highly concentrated samples has been developed to bring the concentration into the optimal range for measurement. In addition to diluting samples, this protocol involves varying the injected sample volume that is loaded into the analyzer as a way of lowering the total DIC needed to be measured. Tests were conducted to measure the DIC of feed solutions synthetically tuned to be in equilibrium with 400 ppm of CO_2 and with Na+ concentration of 2, 5, 10, 20, 50, 100 mM. The DIC analyzer was used to calibrate the inverse ADICM function and confirm that the inverse function resulted in an error of <% for 150 mM alkalinity and lower.

4 CO2 extraction from concentrated solution

An extraction system was assembled to be able to collect and measure the amount of outgassed CO_2 from solution (Fig. 5). Three mass flow controllers (MFCs) were assembled in parallel to deliver mixtures of nitrogen and CO_2 gas at controlled flow rates. The output of the MFCs merge into one gas stream; the gas is wetted through a diH$_2$O bubbler. The gas then flows into the reaction chamber where the solution is exposed to the gas. There are two extraction systems that were tested and calibrated. The first is a simple extraction vessel designed with a syringe for sample loading (Fig. 5B). The second is a gas-liquid exchange membrane, purchased from 3M, which uses hydrophobic materials to create thin channels for the solution to be exposed to gas, thereby increasing the contacting area (Fig. 5C). Both systems were calibrated using the ADICM CO_2 analysis protocol, however, only the extraction vessel was used in the final integration experiments.

4.1 Extraction vessel

CO2 extraction experiments: To calibrate the extraction chamber, we loaded the chamber with 10 mL of synthetic concentrated solution at 1 M, 500 mM, 300 mM, and 100 mM NaHCO$_3$. NaHCO$_3$ was chosen to simulate the maximal DIC concentration for a given alkalinity, with a DIC-to-alkalinity ratio of 1. We then measured the amount of CO_2 extracted into a sweep gas mixture with a CO_2 partial pressure of 50 mbar (Fig 6). We found very good agreement (within $\sim$5%) between the direct gaseous CO_2 measurement, which used an infrared CO_2 sensor to measure the partial pressure in the exit stream over time, and the solution DIC measurement, corroborating both measurement protocols as accurate.
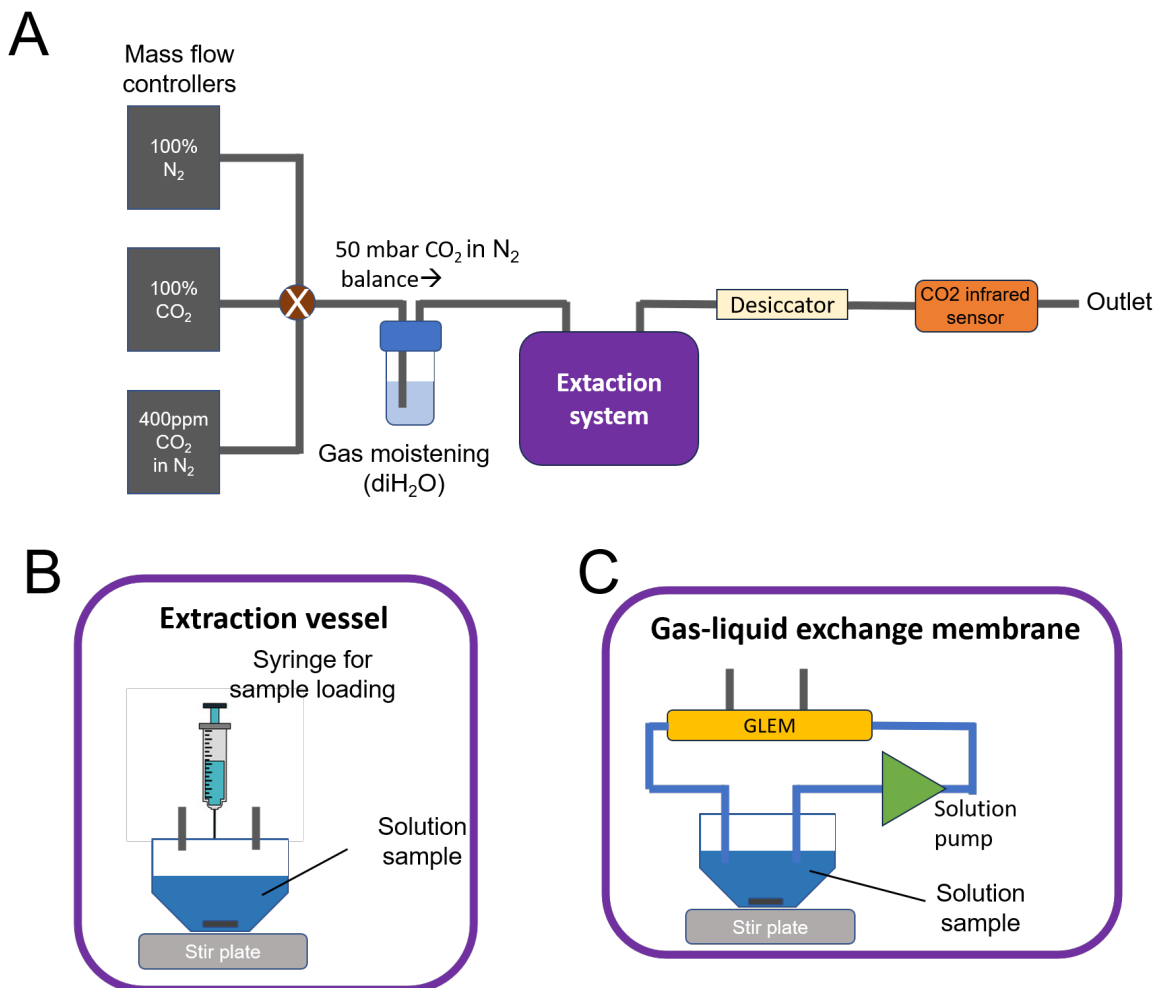
Figure 5: **Extraction schematic.** (A) Schematic of extraction system. (B) Extraction vessel with syringe sample loading system. (C) Gas-liquid exchange membrane system.

4.2 Gas-liquid exchange membrane

Gas-liquid exchange membranes were tested in the extraction system. Five conditions were tested at 100, 300, 500, 1000 mM sodium bicarbonate concentration, and 2000 mM potassium bicarbonate concentration. Figure 7 plots the headspace partial pressure of CO_2 during outgassing into a 50 mbar stream over time. The table in Figure 7 compares the outgassed concentration to the extraction vessel testing demonstrated in Figure 5. Outgassing measurements are in good agreement across both systems.

5 Dilution and re-equilibration with air

The absorption rate associated with a given direct air capture process is a crucial figure of merit that will correspond to the amount of contacting infrastructure for an aqueous-based approach. For an aqueous alkaline process, CO_2 enters solution and reacts to form a bicarbonate ion, either through binding with a hydroxide or by reacting with water and disassociating a proton. The hydroxide pathway is dominant at high pH (above 9), and, in general, the absorption of CO_2 into aqueous alkaline solution has been the subject of extensive study.[8]

5.1 Extraction vessel calibration

Protocol:
- Inject 10 ml of NaHCO3 solution into vessel
- Expose to 50 mbar of CO2 in 950 mbar N2 balance at 2000 sccm gas flow
- Measure CO2 percent relative to 50 mbar baseline
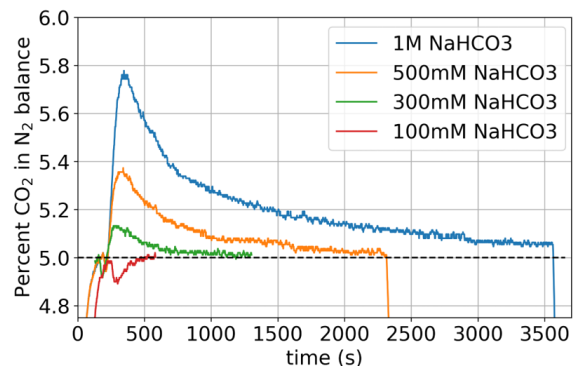
Solution measurement (PHREEQC)

Initial Alkalinity (M)	Initial DIC (M)	pH post-outgassing	DIC post-outgassing (M)	ΔDIC post-outgassing (mmoles)	Direct gas CO2 outgassing measurement (mmoles)
1	1	8.51	0.895	1.05	1.00
0.5	0.5	8.42	0.468	0.323	0.309
0.3	0.3	8.21	0.291	0.082	0.0667
0.1	0.1	-	-	-	Absorbed CO2

Figure 6: **Extraction vessel calibration.**

5.2 Gas-liquid exchange membrane calibration
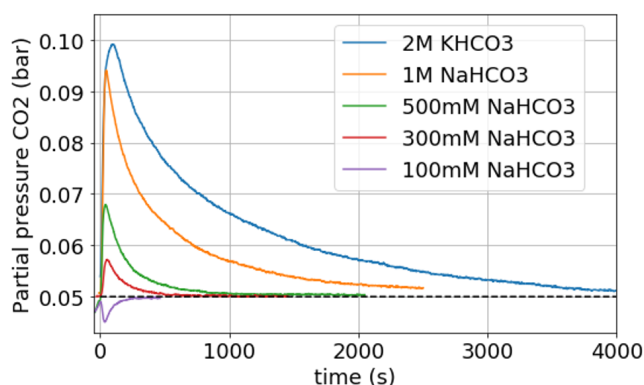
Protocol:
- Add 30 ml of NaHCO3 solution in reservoir
- Expose GLEM to 50 mbar of CO2 in 950 mbar N2 balance at 2000 sccm gas flow
- 40 sccm liquid flow through membrane
- Measure CO2 percent relative to 50 mbar baseline

Initial Alk. & DIC (M)	5.1 Vessel extraction (mM)	5.2 GLEM extraction (mM)
2	-	230
1	100	110
0.5	31	27
0.3	6.6	6.7
0.1	-	-

Figure 7: **Gas-liquid exchange membrane calibration.**

9

In 1950, Danckwerts demonstrated that the kinetics of absorption of carbon dioxide into alkaline solutions follows a pseudo-first order irreversible process.[9,10] The rate can be succinctly written down as follows:

$$J_{CO_2} = p_{CO_2} K_H \sqrt{D_1 k \{OH^-\}} \tag{1}$$

Here, J_{CO_2} is the flux of CO_2 in units of moles per meter squared per second. p_{CO_2} is the partial pressure of CO_2 in the gas phase, K_H is Henry's Law constant, D_1 is the diffusion constant of CO_2 in solution, k is the reaction rate constant between hydroxide and CO_2, and $\{OH^-\}$ is the activity of hydroxide. This relation is more complicated than it appears, however, as Henry's constant, the diffusion coefficient, and hydroxide activity all depend on various solution properties such as ionic strength, temperature, and presence of other species. We modify the Danckwerts equation to consider the partial pressure of the solution, as well as the gas: $p_{CO_2} \rightarrow p_{CO_2}^{gas} - p_{CO_2}^{sol}$, where the "gas" and "sol" superscripts, correspond to the CO_2 partial pressure in the gas and solution phases, respectively.

Various studies have experimentally and theoretically investigated the CO_2 absorption process. Stolaroff et al. (2008) reported a spray setup to test absorption of CO_2 through aerosolized sodium hydroxide droplets. Carbon Engineering reported their operating condition at 1 M hydroxide concentration, though the exact contacting design is not publicly known.[11,12] Promoter molecules such as amines,[13] boric acid,[14] and enzymes, such as carbonic anhydrase,[15-17] have been explored as a way to enhance CO_2 flux.[18,19]

Unlike that of Carbon Engineering and other high pH processes (>12), the alkalinity concentration swing outgasses through disproportionation of bicarbonate ions, and thereby necessitates the presence of bicarbonate in the contacting solution. This, in turn, implies that the contacting pH likely has to be lower than 11, even with the enhancement from bicarbonate enrichment. Taking the square root Danckwerts relation as a heuristic, an ACS process operating at pH 10 would be 100 times slower than a pH 14 process. Therefore, for the ACS to reach comparable absorption rates, some promoter molecule must be introduced.

Certain promoter molecules, such as the enzyme carbonic anhydrase (CA), increases the rate of the following water solvation pathway:

$$CO_2(aq) + H_2O \leftrightarrow HCO_3^- + H^+ \tag{2}$$

5.1 Materials and methods

To study absorption and outgassing rates, a stirred-cell reactor (SCR) setup was assembled (Fig. 8). Three mass flow controllers (Sierra SmartTrak 50) were installed in parallel, each connected to its own gas tank: 100% N_2, 100% CO_2, 0.4 mbar CO_2 in N_2 balance. Gas tanks were purchased from AirGas. Gases were combined and mixed at a known ratio and flow rate, and bubbled through deionized water, moistening the gas feed and reducing evaporate loss. The gas line is then fed into the SCR, which was installed with conductivity, temperature, and pH probes (ThermoFisher). The SCR was placed on a stir plate and a medium-sized stir bar was spun at 200 rpm. This rpm was chosen so as not to deform the solution surface, but still to be fast enough to achieve a well-mixed solution condition so as to reach the pseudo-first order absorption regime. At 50 mL of solution loading, the gas-liquid surface area was measured to be 0.0029 m^2.

For each experiment, 50 mL of solution was loaded into the SCR, and temperature was controlled at 25C using a water jacket connected to a temperature-controlled water bath. Measurements were continuously recorded onto a computer for analysis. The known solution alkalinity allowed for using pH to calculate CO_2 absorption. Gas flow rates were always high enough to deviate in CO_2 concentration by <5% due to absorption. Conductivity measurements were used to ensure that evaporative loss was within <5%.
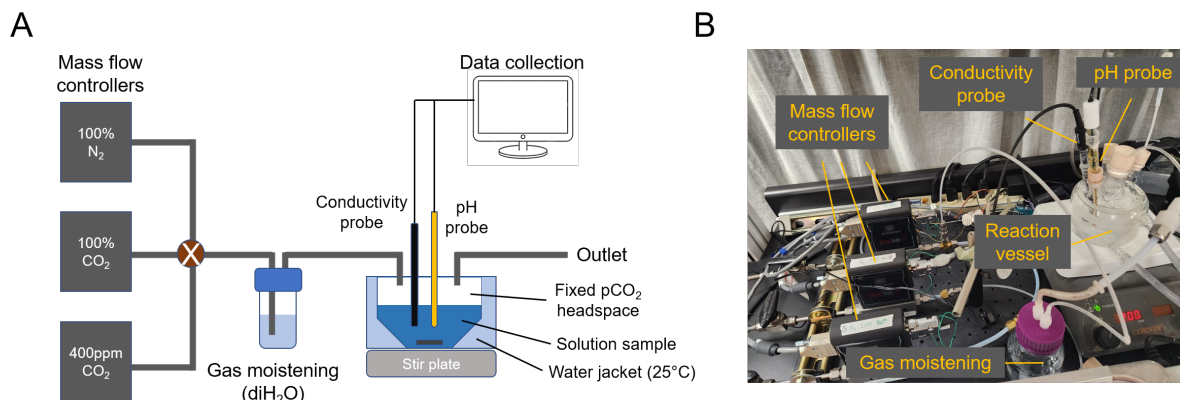
Figure 8: **Absorption and outgassing setup.** (A) Schematic of the absorption and outgassing setup demonstrating the gas and liquid handling. (B) An image of the experimental setup.

5.2 Absorption

We studied the absorption rate of aqueous alkaline solution to confirm that our experimental setup matches the Danckwerts relation. Figure 9 plots the flux of three alkalinity conditions as functions of pH. The 100 mM alkalinity condition varied from pH 12 to below 10, approaching equilibrium with 0.4 mbar CO_2 headspace, validating the modified Danckwerts relation. Rates for the 300 mM and 1 M conditions were measured around pH 11, but long-time equilibration experiments were not pursued.
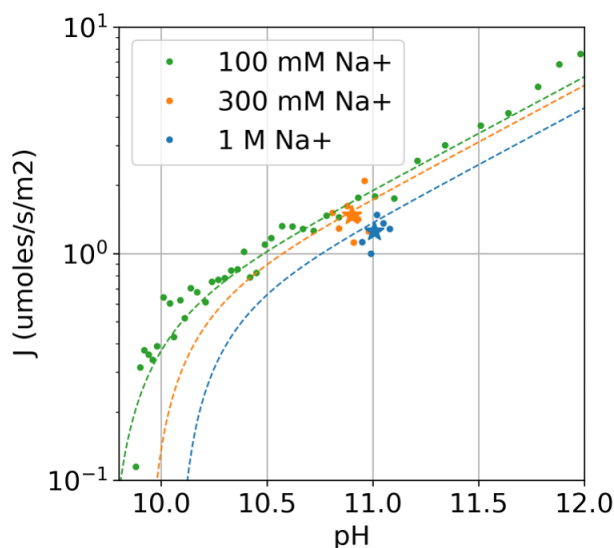
Figure 9: **Experimental confirmation of Danckwerts relation.** Stars correspond to average J values over the pH range studied for the 300 mM and 1 M conditions. Dashed lines correspond to Danckwerts model.

6 Driving the ACS through Reverse osmosis

The core driver of the ACS is an osmotic swing that concentrates and dilutes solutions. Many approaches are able to achieve concentration swings, however, few are as technologically developed and energetically efficient as reverse osmosis.

Reverse osmosis (RO) is a membrane-based separation process in which osmotic pressure is applied against a solvent-filled solution to create a concentrated and a dilute stream. RO is the dominant technology used for seawater desalination. It is also used for brackish water (low salinity) and wastewater treatment, among other applications. The RO industry has benefitted from over 50 years of technological development, and currently produces more than 100 million cubic meters of purified water per day.[20] Seawater desalination plants, in particular, are typically designed to process 600 mM of NaCl equivalent salt and produce two roughly equal flow streams, one purified and one twice concentrated. Such processes are designed for a single-pass process, after which the purified stream output of the RO module is consumed and the concentrated brine solution is discarded.

The high energy efficiency of the RO process makes it an appealing candidate for a swing-driving mechanism. In large part, RO energy efficiency is due to the incompressibility of water. It is possible to apply high pressure on water without it significantly changing volume or undergoing a phase transition, thereby limiting dissipation. The result is that some of the highest efficiency commercial RO plants require only 1.5 to 2x the thermodynamic minimum energy of separation.[21]

It is uncommon for RO modules to be part of a process in which the output solution is recirculated in a continuous closed loop, as would be the case with the ACS. And so worth noting that re-circulation allows for the possibility to recover energy from salinity gradients, such as through forward osmosis modules[22] as well as reverse electrodialysis.[23, 24]

In this section, the concentration step of the ACS process is experimentally investigated. A low-flow bench-top RO setup is used to produce a concentrated solution plug. The permeate stream is continuously monitored to evaluate the state of the DIC solution in the cell. Rejection of DIC species is quantified, target ACS process parameters are characterized, and process limitations are discussed. Energy is briefly considered, but quantification is left for subsequent work, as the benchtop experimental setup that we purchased is not designed with energy efficiency as a consideration.

6.1 Materials and methods

A custom bench-top alkalinity concentration swing reverse osmosis (ACS-RO) set up was assembled for this work (Fig. 10). A cross-flow stainless steel cell, the CF042SS, was purchased from Sterlitech. The cell was connected with stainless steel tubing to a HPLC pump, purchased from Analytical Scientific Instruments (Pump part number: 540-0040, Semi-Prep SST). This pump can reach pressures of 3500 PSI, but unlike traditional high pressure and high flow rate pumps used for RO, this pump operates in a low-flow constant flow rate regime (0-40 mL/min). The reason for this experimental setup choice was to allow for a maximizing the single-pass concentration factor within the cell, which would not be possible with high flow rates. This allowed for testing the membrane properties over a a wide range of feed conditions, as well as monitoring the concentrate DIC solution throughout the concentration process.

A high-performance candidate membrane was chosen for all experiments: Toray UTC-82V. Its commercial specifications are rated for high rejection seawater operations, operating in a 2-11 pH range, 29-40/150 flux of gallons / square foot / day per PSI, salt rejection of 99.5-99.7%, and a polymer of Polyamide-TFC.

In-line conductivity and pH were used to continuously measure both the permeate output and the concentrated plug output. The following probes were purchased from Atlas Scientific: Atlas Scientific Mini Conductivity Probe K 1.0 and Mini pH Probe 0-14. Conductivity, pH, and temperature measurements allow for inferring the alkalinity and DIC concentration of solution, based on the Aqueous DIC Model.

Unless otherwise stated, the following experiment protocol was used (Fig. 11):

ASI high-pressure pump:
Constant flow condition
Flow rate: 0-40 ml/min
3500 psi max
Continuous digital pressure reading
P_{max} sets shut off pressure for pump

CF042 Cell specs:
Membrane area: 42 cm2
Hold-up volume: 17 ml
Typical permeate: 2-20 mL/min
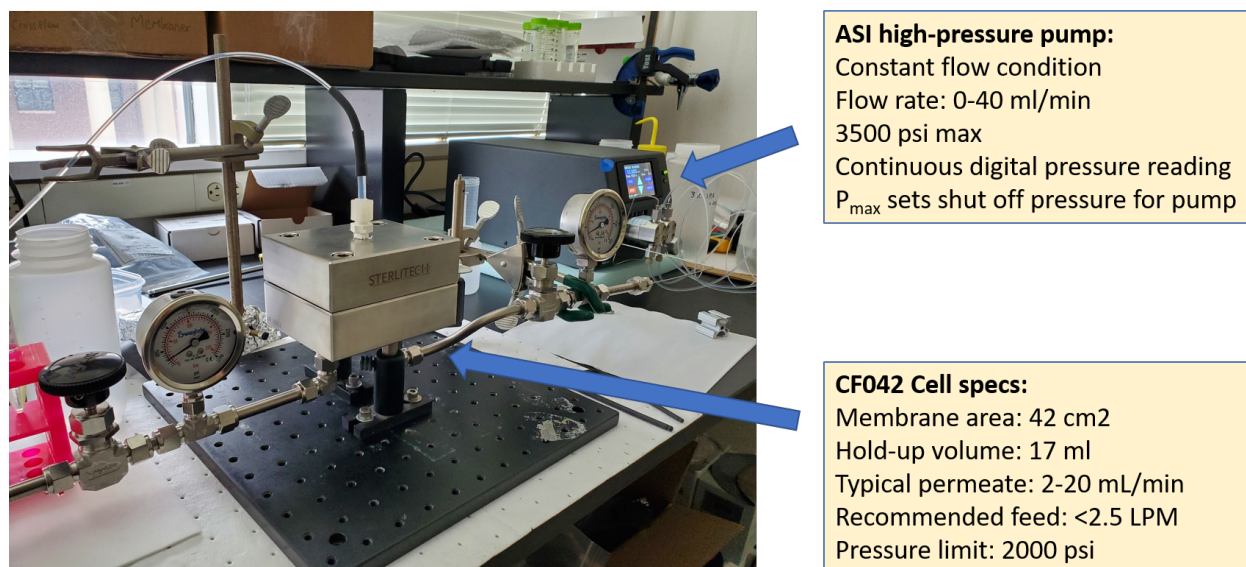Recommended feed: <2.5 LPM
Pressure limit: 2000 psi

Figure 10: **ACS-RO setup.** High pressure, low-flow pump feeds solution into the reverse osmosis cell. Pressure is regulated by down-stream pressure regulators. Permeate and concentrate lines pass solution through in-line pH and conductivity sensors (not shown).

1. **Concentration step**: Close concentrate line and flow feed for 1 hour at 1-3 mL/min in a dead-end regime. Pressure builds as concentration in cell increases. Conductivity and pH are continuously measured in the permeate stream.

2. **Switch-over**: Turn off flow and open concentrate line letting internal cell pressure return to 1 bar.

3. **Plug measurement**: With concentrate line open, push plug of concentrate at a fixed flow rate through in-line conductivity and pH probes to quantify DIC and alkalinity concentration.

6.2 ACS-RO system and membrane characterization

6.2.1 Pressure-flow rate relation

The RO system was first characterized by feeding deionized water and solution at different salt concentration at different flow rates.

Due to the dead-end nature of this experimental configuration, there is essentially no cross-flow component across the membrane. This results in a possible significant concentration polarization effect.[25] However, the extremely low flow rate reduces the concentration polarization effect, which scales with the membrane flux (J_w): $\sim e^{J_w/\kappa}$. Here, κ is a the mass-transfer coefficient, not explicitly evaluated for our system.

Given the membrane surface area of 42 square centimeters, a flow rate of 1 mL per minute in a dead-end configuration means that the trans-membrane velocity is 40 mm per second. In liters per squared meter per hour this value is 14 LMH. This is significantly lower than many RO and nanofiltration membrane operations, which tend to exceed 100 LMH.

To understand the relationship between pressure and flow rate, deionized water was first fed into the RO system at varying flow rates and the pressure was measured. Figure 12A plots gauge pressure in PSI as a function of time for 3, 5, 6, and 7.5 mL per minute conditions. Because the system is in a dead-end configuration, pressure builds rapidly and then stabilizes once the pressure drop over the membrane is established allowing for water permeation. For

13
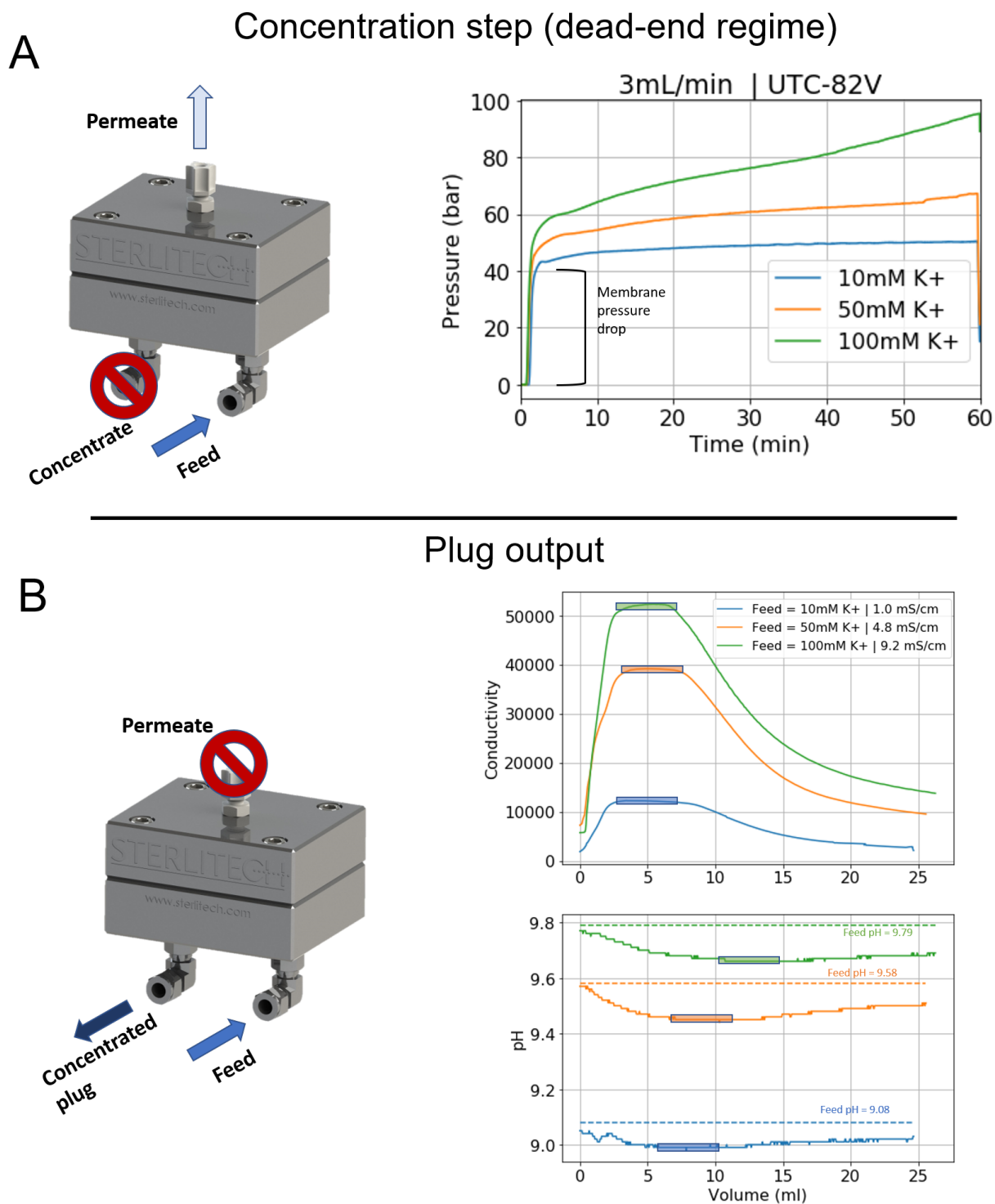
Figure 11: **Concentration protocol.** (A) During the concentration step, the concentrate line is completely shut off, dead-ending the cell and resulting in building pressure as solution is permeated and internal cell concentration increases. (B) Once a target amount of solution is permeated through the cell, the permeate line is closed and the concentrate line is opened, relieving the internal pressure. The concentrate plug within the cell is pushed out at a fixed flow rate through in-line pH and conductivity sensors (right panel).

these flow rates, pressure stabilizes roughly at 600, 800, 1000, and 1300 PSI, respectively, and then slowly builds due to increasing salt concentration. The pressure drop depends on membrane properties as well as flow rate.

14

When the feed contained 50 and 100 mM of NaCl, stabilizing pressure increased due to the additional osmotic pressure of the dissolved solutes (Fig. 12B) Pressure curves were reproducible over multiple cycles; however, different membrane sheets (even if the same brand from the same manufacturer) yielded slightly different characterization values, while reproducing the qualitative behavior. Variation is expected due to membrane inhomogeneity, and the exact membrane properties are not of particular concern beyond the ability of the membrane to achieve high salt rejection.
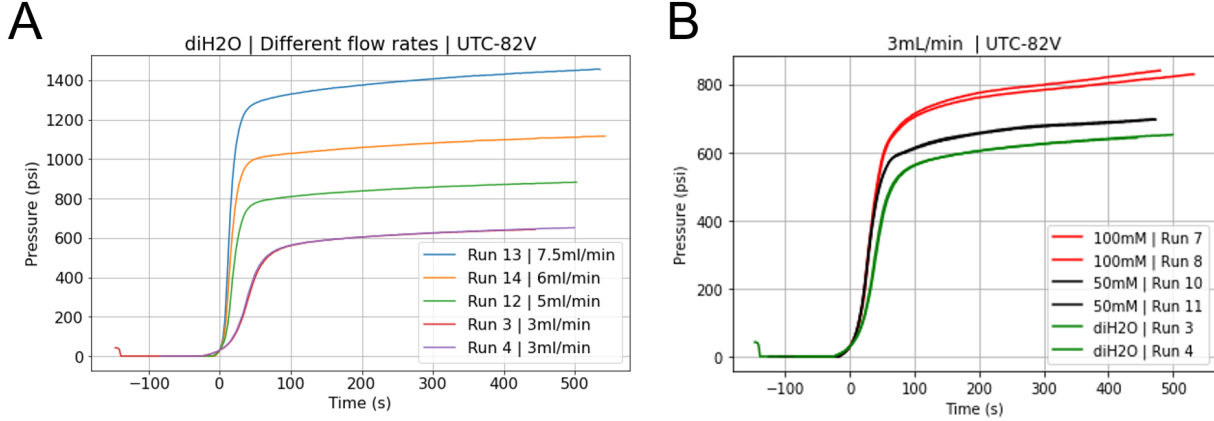

Figure 12: **ACS-RO pressure characterization.** (A) Gauge pressure vs. time for deionized water permeating in the dead-end configuration through the UTC-82V membrane at various flow rates. (B) Gauge pressure vs. time for a 3 mL/min permeation rate for deionized water and for 50 mM and 100 mM of NaCl.

6.2.2 Membrane characterization

To characterize membrane conditions, a stirred cell (HP4750 purchased from Sterlitech Inc.) was used to increase the cross-flow and reduce concentration polarization effects. Figure 13A plots the Toray UTC-82V membrane salt rejection coefficient for bicarbonate and carbonate ions for different feed DIC-to-alkalinity ratios, all at 50 mM Na^+ concentration. Salt rejection coefficients are determined using the following equation:

$$\Gamma_i = 1 - \frac{ln(1 - \Phi C_{2,i}/C_{1,i})}{ln(1 - \Phi)}. \tag{3}$$

Here, C_i is the concentration of species i with the subscript 1 signifying the feed and subscript 2 signifying the permeate. Φ is the permeation volume fraction, and Γ_i is the rejection coefficient, which is assumed to be constant for a given membrane across concentration conditions.

On average, across the DIC-to-alkalinity conditions, the rejection coefficient of alkalinity (i.e. sodium cations, in the case at hand), is found to be: $\Gamma_A = 99.10 \pm 0.11\%$. The average carbonate rejection coefficient is $\Gamma_c = 99.75 \pm 0.09\%$ (Fig. 13A inset). The bicarbonate rejection varies as a function of DIC-to-alkalinity, reaching as low as 90% close to 0.5 and up to around 99% closer to 1.

Importantly, aqueous CO_2 is expected to be unaffected by the reverse osmosis membrane. Dissolved gases, in general, as neutral species, have been shown not be blocked by RO systems.[26] This implies that at high DIC-to-alkalinity ratios, where higher aqueous CO_2 concentrations are present, CO_2(aq) will permeate freely through the membrane. This effect is studied in detail in the next section.

Finally, it is worth noting that while the rejection coefficient is high for both bicarbonate and carbonate, the relative rejection varies with feed pH and, thereby, with the DIC-to-alkalinity ratio. The bicarbonate-carbonate selectivity factor captures this variation, and is calculated as follows: $S_{b,c} = \frac{1 - \Gamma_b}{1 - \Gamma_c}$.

Figure 13B plots $S_{b,c}$ as a function of pH, and shows that selectivity is roughly around 10 for lower pH, increasing to values closer to 30 around pH 11.
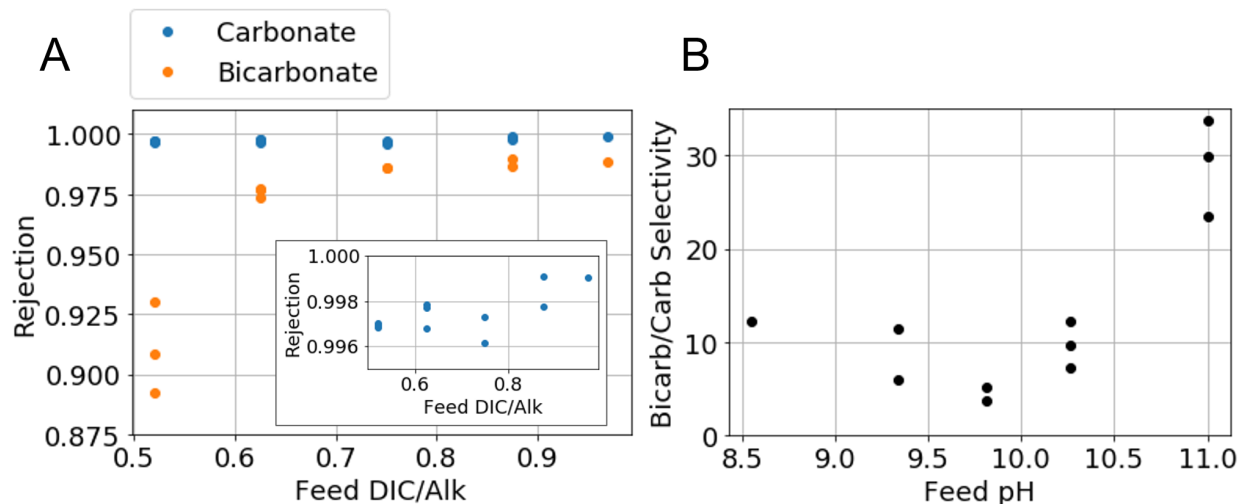

Figure 13: **RO membrane characterization.** (A) Rejection of carbonate and bicarbonate ions as a function of feed DIC-to-alkalinity. Inset plots carbonate ion rejection with rescaled y-axis. All feed conditions are at 50 mM Na$^+$. (B) The same data, plotted as bicarbonate-carbonate selectivity factor as a function of feed pH.

This rejection analysis demonstrates the ability for reverse osmosis membranes to exhibit rejection coefficients above 99% and to be used to concentrate alkalinity and DIC ions. It also reveals that carbonate rejection is significantly higher than bicarbonate rejection, likely due to their respective divalent and monovalent charges. It is expected that industrial systems, whose geometry, flow, and pressure parameters are engineered and optimized, will be able to achieve higher rejection coefficients than the values reported in this work.

6.3 Results

6.3.1 Conductivity and pH measurements

The rejection of >99% demonstrated in the RO setup allows for experimentally testing the ACS concentration step. 9 feed solutions were prepared, spanning two alkalinity conditions and varying the DIC-to-alkalinity ratio from 62.5% to 100%. High DIC-to-alkalinity conditions test low pH regimes with high CO_2(aq) concentration. Low DIC-to-alkalinity conditions test higher pH regimes where lower concentrations of CO_2(aq) are present.

Figures 14 and 15 plot the measured conductivity and pH of the 50 mM and 150 mM feed alkalinity (Na$^+$) concentration conditions, respectively. The permeate stream measurements are plotted in panels A, and the concentrate plug measurements are plotted in panels B. A limitation of this experimental setup is that for roughly 20 mL of the initial permeate measurements, the solution measurements are still stabilizing and are affected by the previous run. However, this limitation does not change the overall analysis and interpretation of the data, as stable conductivity and pH readings can be taken indefinitely after the initial stabilization period. In some cases, pH readings take longer to reach steady state, likely due to DIC speciation kinetics. The concentrate plug conductivity profile is highly reproducible between runs.

An immediate observation for both the 50 and 150 mM experiments is that the conductivity magnitude and trend over time are independent of the DIC-to-alkalinity ratio, while the pH curves have a strong dependence. For the 50 mM condition, permeate pH varies from around 6 to 9.5 as the DIC-to-alkalinity ratio is varied from 1 to 0.625. For the 150 mM condition over the same DIC-to-alkalinity range, permeate pH varies from below 6 to close to 10. This

suggests that the DIC speciation is strongly affected by the feed condition. The change in pH between the feed and the permeate is largest in high DIC-to-alkalinity regimes. For example, for 150 mM 100% DIC-to-alkalinity feed, the pH is reduced by more than two pH units from around 8.3 down to 6; for 150 mM 92% DIC-to-alkalinity feed, the pH is reduced from around 9 to 6.5 (Fig. 15).
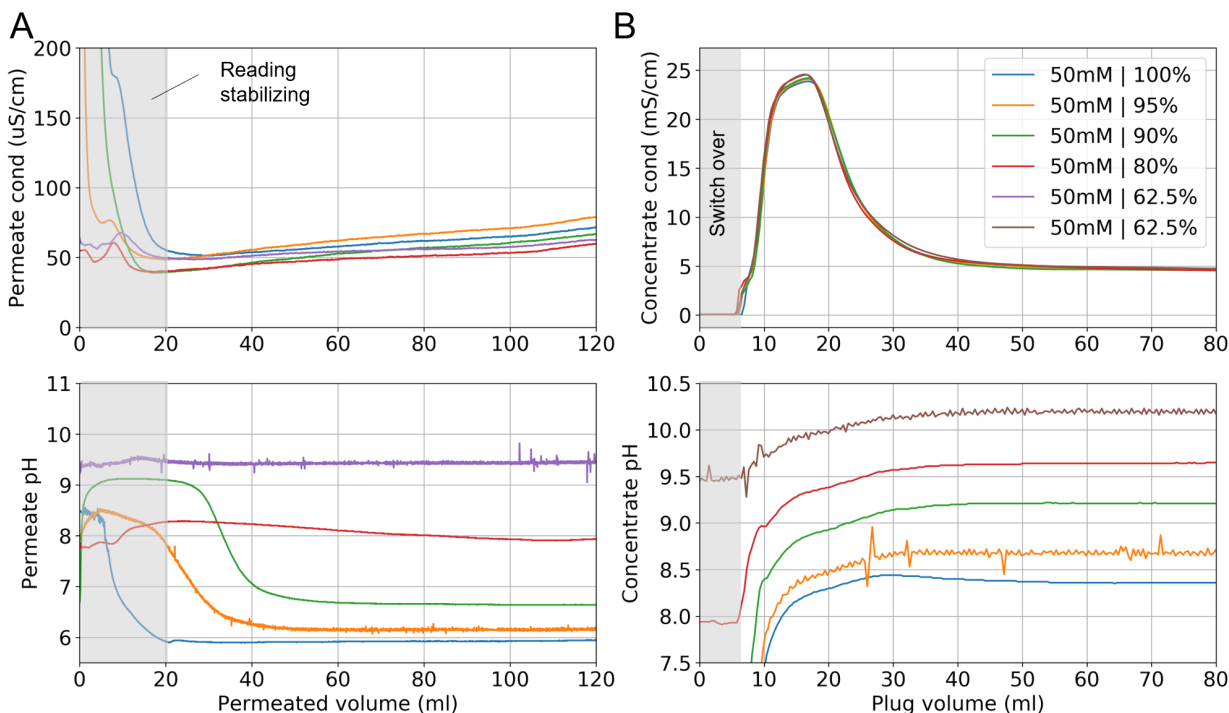

Figure 14: **Permeate and plug data for 50 mM feed.** (A) Permeate conductivity (top) and pH (bottom) measurements as functions of permeated volume. Sensor readings are stabilizing for the initial 20 mL of solution. Colors correspond to different DIC-to-alkalinity feed conditions. (B) Concentrate plug conductivity (top) and pH (bottom) measurements as functions of plug volume. Initial several mL correspond to a switching regime between the permeation and plug reading. All experiments are conducted at 2 mL/min for 1 hour.

6.3.2 Permeated DIC analysis

Using the Aqueous DIC Model, the conductivity, pH, and temperature measurements of the permeate can be transformed to concentrations of alkalinity, bicarbonate, carbonate, and aqueous CO_2 as functions of permeated volume. Figure 16 plots the species concentration for each DIC-to-alkalinity ratio of the 50 mM feed solution: 62.5, 80, 90, 95, and 100%. Figure 17 plots the species concentration for each DIC-to-alkalinity ratio of the 150 mM feed solution: 62.5, 80, 92, and 100%.

Whereas at low DIC-to-alkalinity ratios, carbonate and bicarbonate species are present, at high DIC-to-alkalinity ratios, bicarbonate and aqueous CO_2 species are present. Substantial aqueous CO_2 concentrations are not observed at 80% DIC-to-alkalinity, but emerge at 90% and above. All species concentrations increase with increasing permeated volume due to the accumulating concentration within the RO cell as more feed solution enters.

Interestingly, the permeate alkalinity is slightly less than 1% of the feed concentration, but increases by only a factor of less than 2, even though the concentration factor of the solution within the cell reaches around 8. This suggests that concentration gradients within the cell exist and allow for feed to permeate without fully mixing with the concentrate.
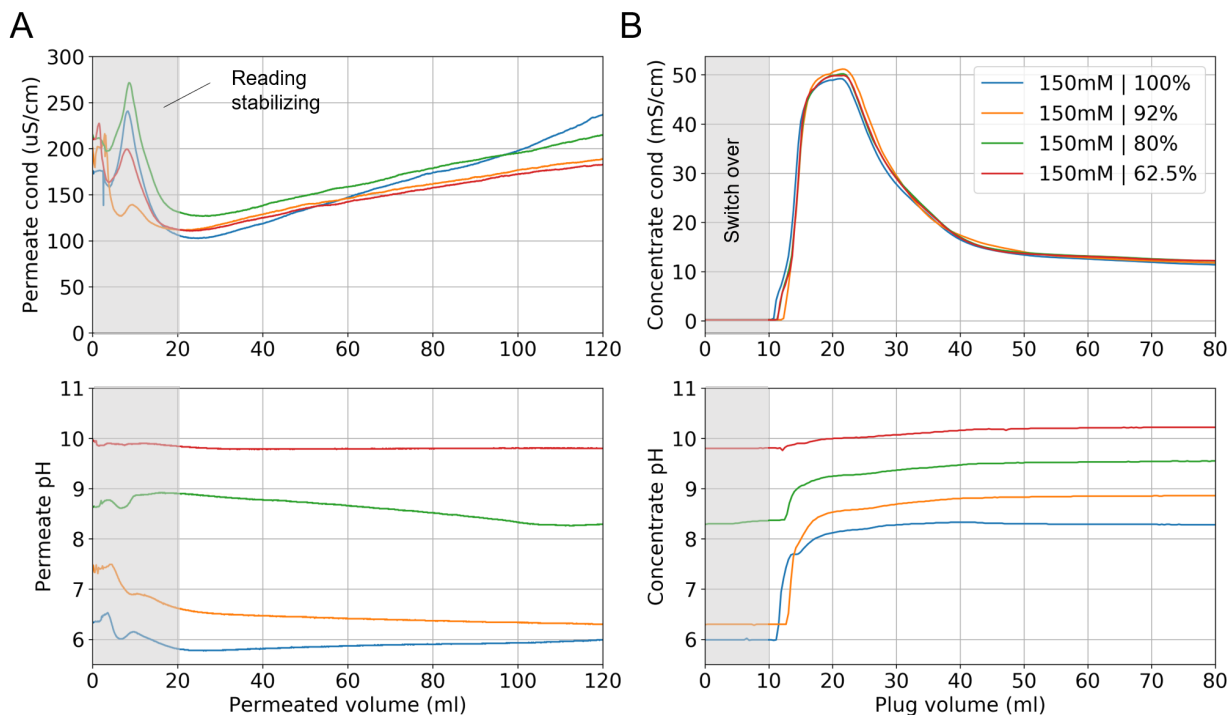
Figure 15: **Permeate and plug data for 150 mM feed.** (A) Permeate conductivity (top) and pH (bottom) measurements as functions of permeated volume. Sensor readings are stabilizing for the initial 20 mL of solution. Colors correspond to different DIC-to-alkalinity feed conditions. Legend reports the initial alkalinity and the percentage of DIC-to-alkalinity at the feed. (B) Concentrate plug conductivity (top) and pH (bottom) measurements as functions of plug volume. Initial several mL correspond to a switching regime between the permeation and plug reading. All experiments are conducted at 2 mL/min for 1 hour.

The key finding in these experiments concerns the dynamics of aqueous CO_2. Specifically, the permeated aqueous CO_2 can increase significantly through the concentration process. This is due to the fact that, as concentration builds within the cell, DIC speciates and higher aqueous CO_2 concentrations are produced at higher alkalinity concentrations.

Figure 18 plots the partial pressure of CO_2 for all experiment conditions, revealing both the increase in p_{CO_2} through the concentration process, as well as the difference in p_{CO_2} as a function of DIC-to-alkalinity ratio. In the 150 mM 100% condition, CO_2 partial pressure exceeds 100 mbar, with aqueous CO_2 reaching >7.5 mM.

6.3.3 Total permeated alkalinity and DIC

Integrating the total amount of DIC and alkalinity permeated through the system reveals a strong dependence on permeation fraction as a function of the feed DIC-to-alkalinity. Figure 19 plots the alkalinity and the DIC moles permeated over the 120 mL of solution passed for the 50 and 150 mM feed conditions. Alkalinity permeated is approximately independent of feed DIC-to-alkalinity, resulting in an average alkalinity rejection of 98.8% for the 50 mM condition, and 98.9% for the 150 mM condition. These percentages were determined by comparing the total permeated salt to the expected total salt in the feed over the entire permeation run. DIC permeation, on the other hand, increases as feed DIC-to-alkalinity increases. This is due to the increase in the uncharged DIC species, aqueous CO_2, which does not get blocked by the RO membrane. The permeated DIC-to-alkalinity ratio as a function of feed DIC-to-alkalinity ratio follows the same trend increasing from slightly below 1 at 62.5 % to above 4 at 100 % (Fig. 19C).
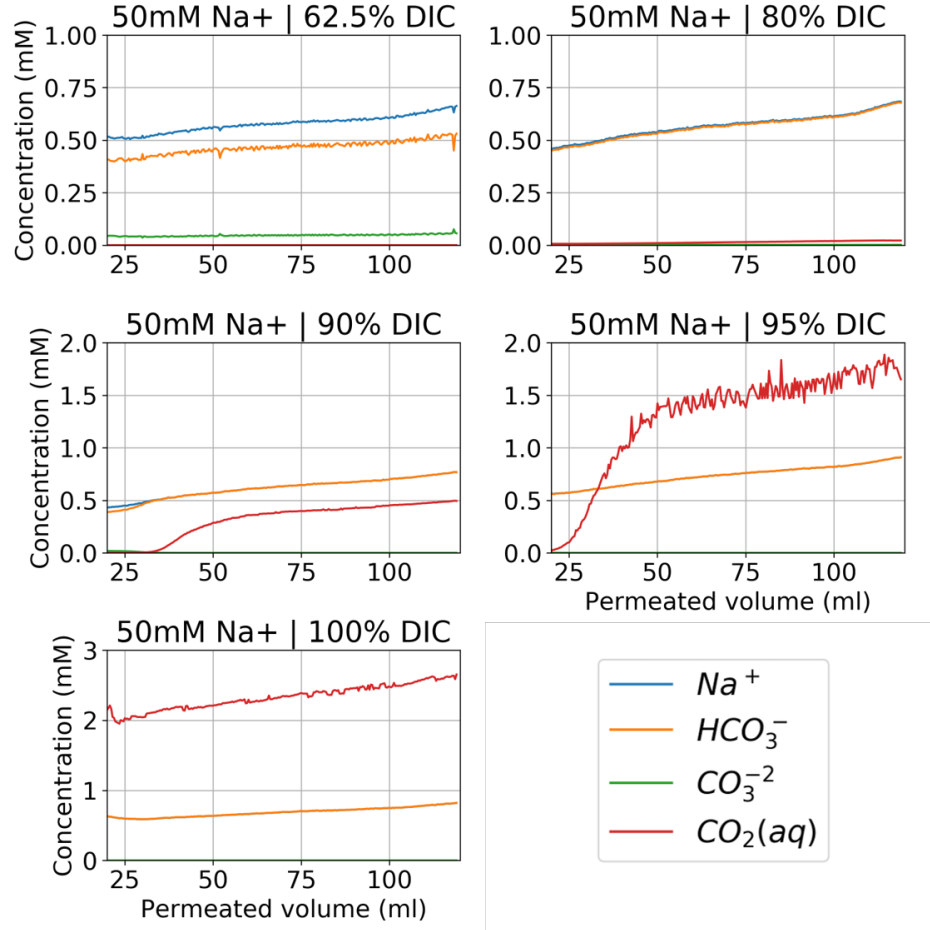
Figure 16: **Permeated concentration for 50 mM feed condition.** Each panel plots the concentration of Na^+, HCO_3^-, CO_3^{-2}, and $CO_2(aq)$ as functions of permeated volume.

6.3.4   Concentrated plug analysis

The concentration experiments for all of the conditions permeating 120 mL of solution (1 hour at 2 mL/min), results in permeated solution stream, as well as a concentrate plug. The high RO membrane rejection around 99% meant that the concentrate build up in the cell increases by almost the exact number of moles that the feed solution brings into the cell.

Figure 20 presents our analysis for the plug alkalinity and DIC concentrations. The alkalinity curves are roughly the same for all DIC-to-alkalinity conditions. In contrast, the DIC curves scale proportionally with the feed DIC-to-alkalinity ratio. The DIC-to-alkalinity ratio of the top 5 mL of the plug (Fig. 20; right panels) is essentially equal to that the feed.

Table 1 reports the resulting concentration factors and increases in partial pressure of the concentrate plug, calculated through the ADICM. For all the 50 mM experiments, the alkalinity concentration factor relative to the feed is: $\chi \approx 7.6$. The highest partial pressure reached is from the 100 % DIC:A solution with the p_{CO_2} changing from 20 to 100 mbar. However, this is only a 5x increase in partial pressure. Lower DIC-to-alkalinity conditions exhibit a partial pressure increase by a factor of closer to 10x. This difference is likely explained by the loss of aqueous DIC to permeation at high DIC-to-alkalinity conditions.
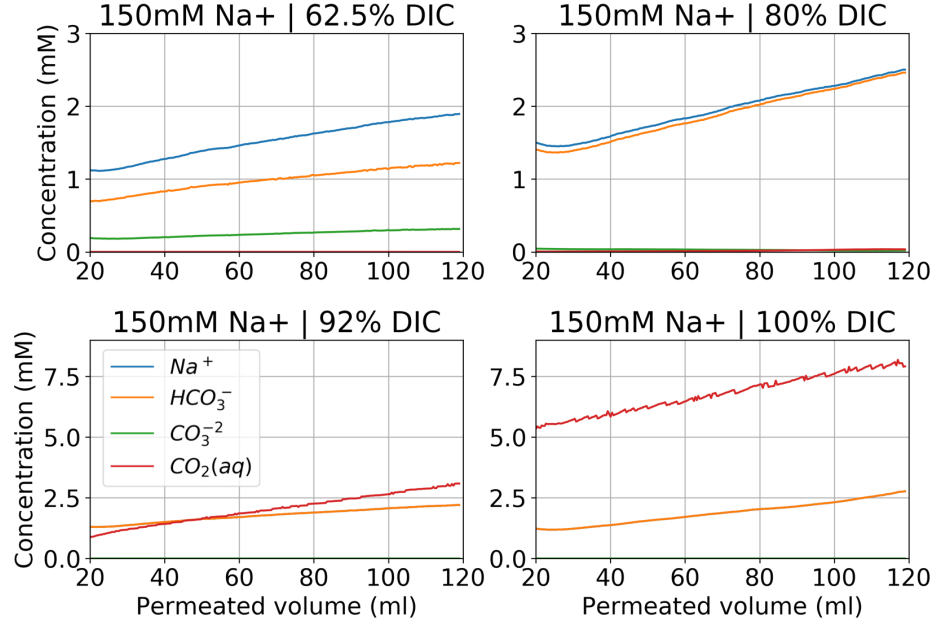
Figure 17: **Permeated concentration for 150 mM feed condition.** Each panel plots the concentration of Na^+, HCO_3^-, CO_3^{-2}, and CO_2(aq) as functions of permeated volume.
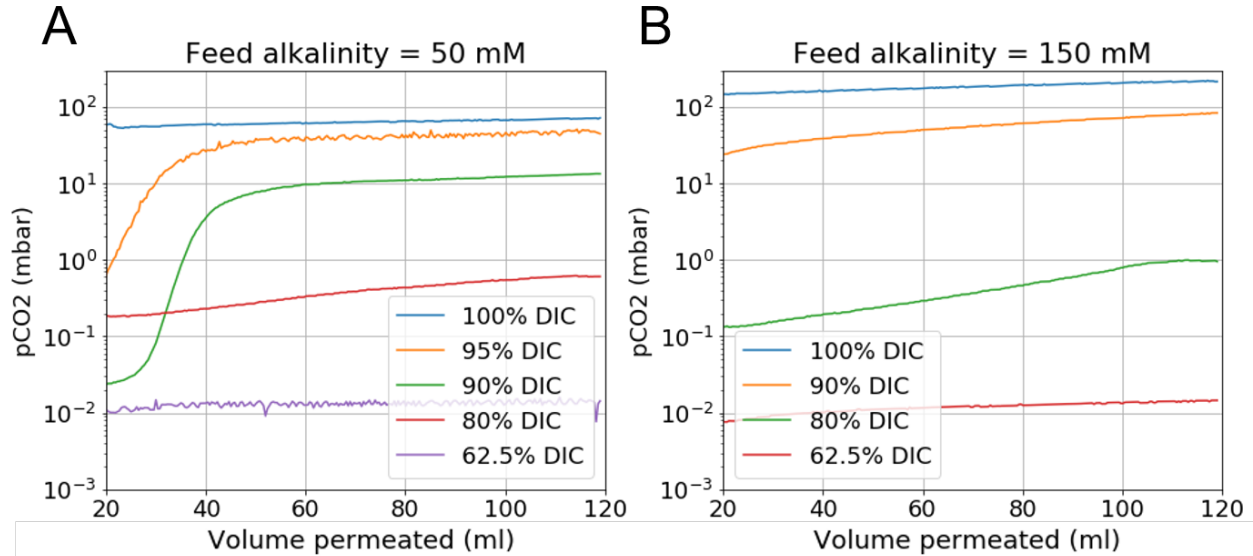
Figure 18: **Permeated CO_2 partial pressure.** (A) Partial pressure of CO_2 in the permeate stream for various DIC-to-alkalinity ratios as functions of permeated volume for the 50 mM feed. (B) Same as (A), but for the 150 mM feed condition.

For all the 150 mM experiments, $\chi \approx 6.5$. The highest partial pressure reached is from the 100 % DIC:A solution with the p_{CO_2} changing from 52 to 240 mbar. Again, lower DIC-to-alkalinity conditions exhibit a higher partial pressure increase factor due to reduced aqueous CO_2 loss.

We also evaluate the theoretical cycle capacity, C_{out}, based on an outgassing pressure of $pCO_2 = 50$ mbar. Only three conditions surpass 50 mbar in the concentrated plug: 50 mM at 100% DIC:A and 150 mM at 92 and 100% DIC:A. This suggests that higher alkalinity feed conditions are preferable starting points and allow for lower DIC-to-alkalinity ratios.

20
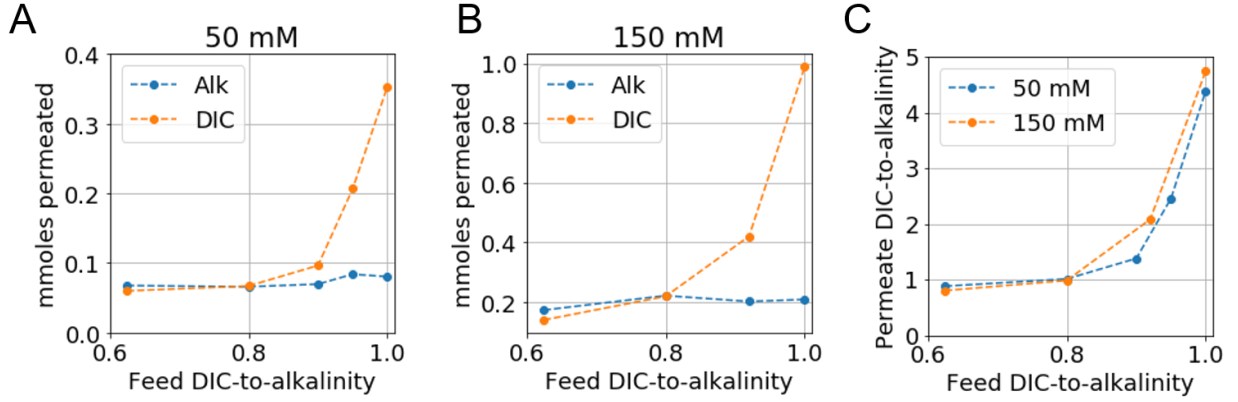
Figure 19: **Permeated moles and DIC-to-alkalinity analysis.** (A) Number of mmoles of alkalinity and DIC permeated over 120 mL of solution passed vs. DIC-to-alkalinity ratio for the 50 mM feed condition. (B) Same as (A), but for the 150 mM condition. (C) Permeated DIC-to-alkalinity ratio vs. feed DIC-to-alkalinity ratio for both the 50 and 150 mM feed conditions.
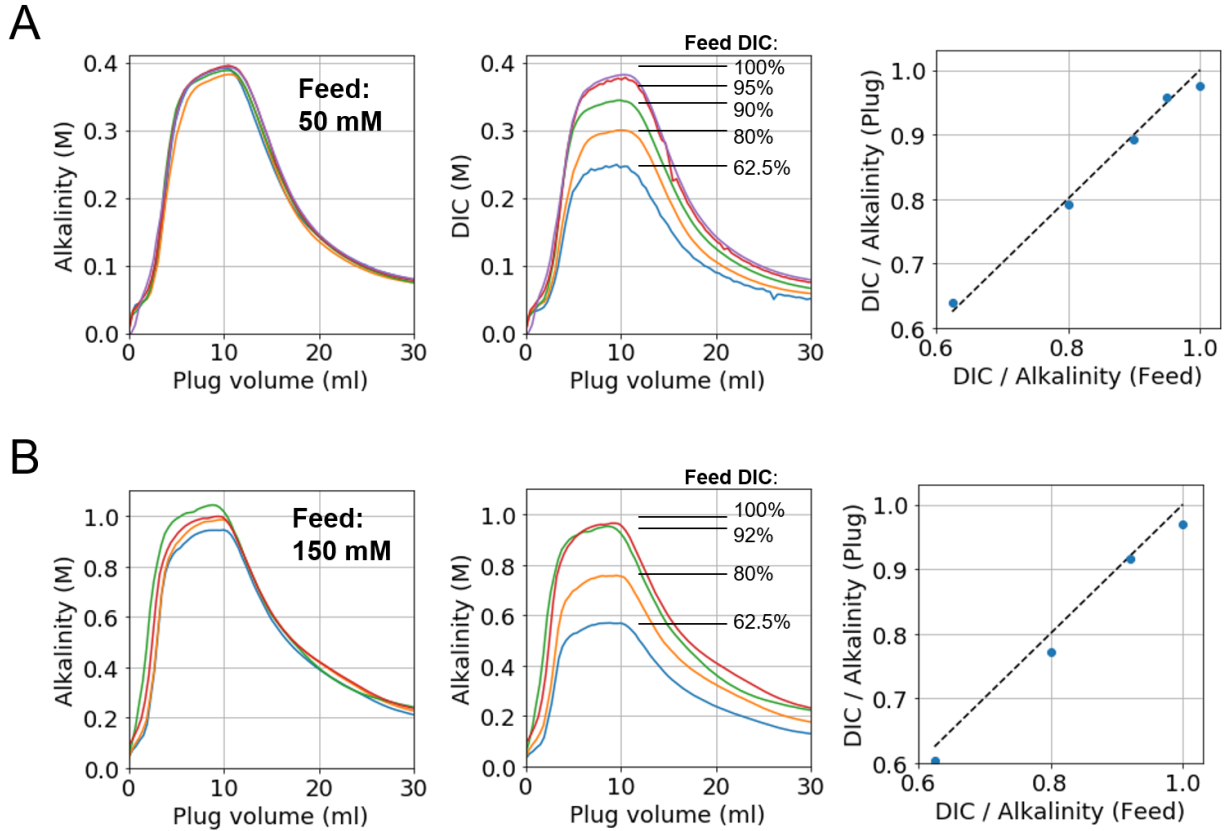
Figure 20: **Concentrate plug analysis.** (A) Plug alkalinity (left) and DIC (middle) concentration for the 50 mM feed condition, as functions of the plug volume passed. Feed DIC-to-alkalinity ratios are labeled in the middle panel. Right panel plots the DIC-to-alkalinity ratio of the 5 mL with the highest concentration as a function of the feed DIC-to-alkalinity ratio. Dashed line is unity. (B) Same as (A), but for the 150 mM feed condition.

Taking the calculated extracted CO_2 quantity per feed volume, or C_{out} value, and combining that with the total permeated volume and the pressure throughout the process allows for an energy calculation: $E_{CO2} = <P>V/C_{out}$, where $<P>$ is the average gauge pressure and V is the volume of permeate. In our system, the 50 mM conditions

operate an average of 35 bar of pressure throughout the process, and the 150 mM conditions operate at an average of 50 bar. The result are energy values that exceed 1500 kJ/mol, which are exceedingly high for any DAC process. However, these values are based on a bench-top experiment not designed for minimizing energy, but rather to study membrane and solution properties.

Table 1: **Concentrate plug analysis.** Concentrate plug analysis is based on the 5 mL with the highest concentration. pCO_2 reported in mbar; C_{out} in mM; E_{CO_2} in kJ/mol. C_{out} is evaluated theoretically based on a $p_{out} = 50$ mbar. *The solution was prepared at 100% DIC-to-alkalinity ratio, but immediate outgassing resulted in an effective 99.2% ratio, lowering the feed partial pressure.

	Feed			Concentrate plug (top 5 mL)					
#	alk. (M)	DIC:A (%)	pCO_2	Alkalinity (M)	χ	DIC (M)	pCO_2	C_{out}	E_{CO_2}
1	0.05	62.5	0.045	0.38	7.6	0.24	0.57	-	-
2	0.05	80	0.51	0.38	7.5	0.30	4.8	-	-
3	0.05	90	1.9	0.38	7.6	0.34	19	-	-
4	0.05	95	4.5	0.39	7.8	0.37	63	-	-
5	0.05	100	20	0.39	7.7	0.38	100	1.4	7640
6	0.15	62.5	0.16	0.94	6.2	0.57	0.73	-	-
7	0.15	80	1.9	0.97	6.5	0.75	11	-	-
8	0.15	92	10	1.02	6.8	0.94	85	4.6	3833
9	0.15	100*	52	0.99	6.6	0.96	240	11.8	1540

6.4   Discussion

We have experimentally demonstrate the use of reverse osmosis to concentrate alkalinity and increase the partial pressure of CO_2. As expected, higher DIC-to-alkalinity feed conditions result in higher final CO_2 partial pressure. Thus, it is desirable to reach high DIC-to-alkalinity feed conditions prior to concentrating. Higher DIC-to-alkalinity feed conditions, however, also result in more permeated DIC, in the form of CO_2(aq), which evades capture.

Simple DIC concentration modelling reveals that the increase in permeated aqueous CO_2 during concentration can be attributed to DIC speciation within the cell as concentration builds. Without further modification, the loss of aqueous CO_2 to permeation through the concentration process is a limitation that decreases the efficiency of the ACS-RO process. However, the high concentration of permeated aqueous CO_2 means that CO_2 can also be extracted from the permeate, and not just the concentrate. Additional outgassing modules would reduce the efficiency loss, especially because high partial pressure permeate conditions, reaching 100 mbar and higher (Table 1), can be achieved if sufficiently high DIC-to-alkalinity feed solutions are prepared.

This limitation and possible permeate outgassing modification should be evaluated in a system-level process analysis that combines the bicarbonate-enrichment module with the ACS concentrating module.

Finally, it is worth noting that the main goal of this study was to evaluate membrane performance and DIC solution behavior in the permeate and concentrate, and not the energy requirement for concentration. Industrial-scale reverse osmosis systems are able to reach energy efficiency levels not even approached by bench-top systems. Further process and thermodynamic modelling can combine the performance metrics established in this work with known energy requirements for RO systems.

7   Driving the ACS through Capacitive Deionization

Here we describe the first experimental demonstration of the alkalinity concentration swing using membrane capacitive deionization (MCDI) to concentrate DIC-rich solutions from an initial alkalinity to a final alkalinity with a higher solution partial pressure of CO_2.

A key shortcoming of the initial ACS framework is that a solution equilibrated with an ambient CO_2 partial pressure does not have a sufficiently high dissolved inorganic carbon (DIC) content to release CO_2 upon concentration,

except for a narrow range of conditions at low initial alkalinity, like the one depicted in Figure 2, for which the amount of CO_2 released is small. For this reason, we will use solutions that are initiated at a much higher DIC content than could be obtained with ambient conditions, to attempt to achieve post-concentration conditions that could have a measurable volumetric cycle capacity, $C_{out} > 0$. As we will see in this section, however, the selectivity of MCDI microporous electrodes for carbonate ions suppresses the efficacy of the concentration step in these experiments such that we are not able to obtain a $C_{out} > 0$. This is because the ACS is driven by the disproportionation of pairs of bicarbonate ions. So as pairs of bicarbonate ions are exchanged for carbonate ions on the electrode during the MCDI adsorption cycle, the overall capacity of the concentration step is reduced. The origin of this selectivity for divalent carbonate ions and how it can be used to enhance the ACS cycle will be explained in Section 8.

7.1 Capacitive Deionization for Ion Selectivity

Capacitive deionization is a method in which voltage is applied across two porous electrodes to remove ions from solution, by creating an electric double layer made up of electrolyte ions.[27] Membrane capacitive deionization (MCDI) makes use of ion exchange membranes, placed between the feed solution channel and the electrode, to increase energy efficiency, electrode lifetime, and ion transport.[28]

Models for capacitive microporous electrodes, used to understand selective ion electrosorption in MCDI systems, typically invoke the Donnan potential.[29] These models have been shown to match experimental data[30] and have been used to understand observed valence-dependent selectivity of divalent anions over monovalent anions.[31] In the MCDI system we describe here, the Donnan potential results in selective electrode binding of divalent carbonate ions over monovalent bicarbonate ions.
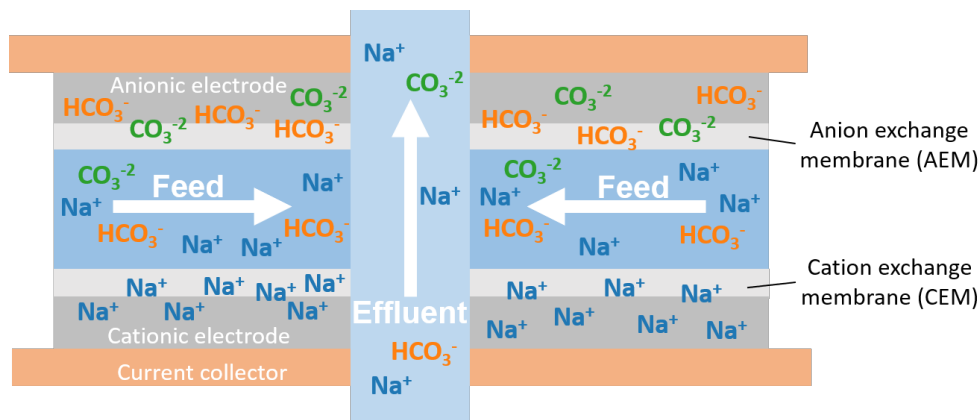
Figure 21: **Membrane capacitive deionization (MCDI) schematic.** A schematic of the charged state of a single MCDI sub-cell. Bicarbonate and carbonate ions are bound to the anionic electrode and odium ions are bound to the cationic electrode.

7.2 Materials and Methods

7.2.1 Solution Preparation

Experiments were conducted at 100 mmolal Na^+ and at three initial DIC-to-alkalinity ratio conditions: 75%, 85%, and 99%. Solutions were prepared by feeding these DIC and alkalinity concentrations into the aqueous DIC model to obtain the quantities of each chemical, sodium carbonate (Na_2CO_3) and sodium bicarbonate ($NaHCO_3$), to add to obtain the correct DIC percentage.

For each condition, we prepared a 10 L reservoir using American Chemical Society-grade chemicals. Beginning with deionized water, Na_2CO_3 was always added first, to minimize the outgassing of CO_2 when $NaHCO_3$

was subsequently added. After addition of both chemicals, the reservoir was immediately sealed and set to stir thoroughly at 200 rpm for at least 2 hours before use in experiments.

7.2.2 MCDI Cell Properties

The CDI cell used for experiments, pictured in Figure 22, is composed of a stack of eight parallel sub-cells, very similar to the cell characterized for NaCl operation by Porada *et al.*[32]
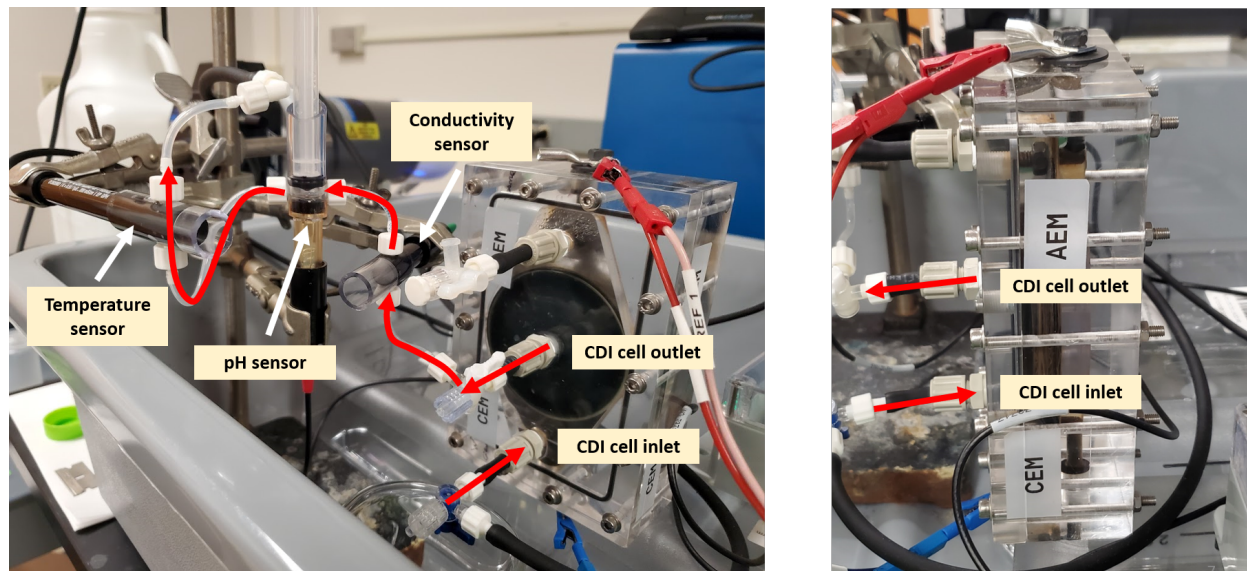

Figure 22: **Membrane capacitive deionization (MCDI) setup. left** Front view, showing the MCDI cell and the pathway of the effluent solution leaving the cell and passing through the 'Effluent Solution Measurement Setup,' which includes conductivity, pH, and temperature sensors. **left** Side view, in which the stack of eight parallel sub-cells that compose the MCDI cell is visible.

Each sub-cell, as shown in the schematic in Figure 21, is made up of a two porous electrodes (Material Methods, Irvine, CA, PACMM^{TM} 203, thickness of $\sim$250 μm) that sandwich a porous polymeric spacer (thickness of $\sim$170 μm), which serves as a flow channel. Each electrode is a circular disk of diameter 6.9 cm with a 1 cm diameter hole cut in the middle (dry weight of electrode pair, m_e = 1.3 g, for a total cell electrode mass of 10.4 g across the eight sub-cells). The spacer is lined by membranes on either side, an anion exchange membrane (Neosepta AMX, Japan) lining the side with the positively polarized electrode (the "anionic electrode") and a cation exchange membrane (Neosepta CMX, Japan) lining the side with the negatively polarized electrode (the "cationic electrode"). Graphite current collectors further sandwich the entire sub-cell.

The current collectors for each sub-cell are bolted together at the top and bottom of the cell, where they connect to the cell's potentiostat leads. The red and blue potentiostat clips can be seen attached to the cell, to the working electrode lead and counter electrode lead, respectively, in Figure 22.

7.2.3 Pump and Reservoir Setup

The cell was operated in a recirculating mode, with the effluent solution during both adsorption and desorption half-cycles being pumped back into a 10 L reservoir. A flow rate of 60 mL per minute was used for each experiment, and the pump was calibrated by manually measuring its flow rate. The same tubing was used for effluent solution to flow back to the reservoir from the effluent solution measurement setup, described in Section 7.2.5.

The reservoir was stirred continuously through experiments at 200 rpm. Solution was pumped from the bottom of the reservoir volume through a frit attached directly to the tubing. Solution was returned to the top of the

reservoir volume. To minimize gas exchange, two holes were drilled into the reservoir to allow the tubing to fit through snugly and the holes were beveled such that O rings could be rolled down the tubing to snugly sit on the beveled edge. Finally, Parafilm was placed around the tubing holes.

7.2.4   Cell Cycling Protocol

Prior to each enrichment experiment, a 0 V desorption step was run to expel any ions accumulated in the prior experiment from the electrodes. This step was run at the flow rate at which the experiment was run, and the step was held until the cell current decayed to a magnitude reached 10 mA, at which point the remaining ions on the electrodes are negligible. After the 0 V desorption step, the cell was left under flow at open-circuit conditions until the conductivity and pH readings became steady, which usually took between 5 and 10 minutes.

Each experiment was run for three cycles, given that conductivity and pH measurements have been observed to converge by the third cycle. Each adsorption half-cycle was run at a constant current of 1000 mA until the voltage reached a cutoff value of 1.2 V. For most experiments described in this section, the constant current step duration was about three minutes, depending on the solution conditions.

After reaching the voltage cutoff, a constant voltage (CV) adsorption step for a particular hold duration was repeated for each of the cycles. For each of the three solution conditions, experiments were run with CV adsorption durations of 1, 5, 10, and 15 minutes. Following each CV adsorption step, a desorption half-cycle was run at a constant current of 1000 mA until the voltage reached a cutoff value of 0 V, and then held at 0 V for 15 minutes.

Thirty seconds prior to the end of the third adsorption step, before desorption began, the flow was turned off. The entirety of the final desorption step then occurred without flow, allowing all of the ions to be expelled into the same static volume within the cell, which we refer to in this section as the "plug." The CV desorption step for the final cycle was held for only 10 minutes, as the peak concentration of the plug was shown to decrease for longer desorption steps, likely because diffusion of the ions throughout the cell volume was more significant at that timescale than the small quantity of ions remaining to desorb from the electrode.

After the final desorption step concluded, the flow was immediately restarted at 6 mL/min and the properties of the plug were measured as it moved through the probe setup, described below.

7.2.5   Effluent Solution Measurement Setup

The effluent solution measurement setup consisted of three probes placed in line after the CDI cell outlet: a conductivity probe, a pH probe, and a temperature probe. These three measurements are required to determine make-up of the solution using the aqueous DIC model, shown in Figure 3. The setup is pictured in Figure 22, where the red line traces the path of the effluent leaving the cell and passing through the probes.

To minimize the volume between the probes, such that the measurements could be as close to simultaneous as possible, a small ID tubing was used. The volume between the cell outlet and the conductivity probe was approximately 0.50 mL, between the conductivity and pH probes was approximately 0.25 mL, and between the pH and temperature probes was approximately 0.50 mL. Because temperature change occurred over the course of hours, and the time to pump through the volume between the first two probes is only roughly 5 seconds at even the slowest flow rate used (7.5 mL/min), no adjustment was made to time series measurements to account for probe separation.

The pH, conductivity, and temperature probes all continuously recorded measurements during experiments. To enable the probes to function as in-line sensors, each was fitted with a short length of tubing that fit snugly around the probe. Holes were drilled into the tubing such that the small segment of tube extending from the female side of a Luer connector fit snugly into the holes. Flow through the conductivity probe bore, which is smooth and does not

accumulate air bubbles, was aligned vertically, bottom-to-top, such that gravity would pull any small air bubbles created during filling through the tubing. The pH probe has a single open face so, to assemble it in an in-line mode, a syringe plunger was placed into the tubing to create a 0.8 mL chamber. Unlike the other conductivity probe, flow through this chamber was aligned horizontally, to ensure that the small air bubbles, which would sometimes accumulate around the plunger head, did not interfere with the measurement. Testing ensured that the pH measurements were still accurate even when the chamber was only half full.

7.3   Results and Discussion

In Figure 23, we plot the raw potentiostat data for the 75% initial DIC-to-alkalinity ratio conditions. Figure 23 A and B show the voltage and current, respectively, for the entire second cycle for experiments of 1, 5, 10, and 15 minute duration adsorption CV steps. Each of these experiments started at the same time but, after a different duration for the adsorption first cycle, their second cycles each started at a different time. For each, we see the adsorption half-cycle, which is cut off at a higher current for all but the longest duration adsorption CV step, followed by the desorption half-cycle, which are all the same duration.

Figure 23 C, D, and E show the voltage, current, and alkalinity, respectively, for all three cycles of the 15 minute adsorption CV step experiment, followed by the post-cycle desorption measurement of the plug. Pane E shows the period when the flow was off and no measurement was being made of the flow channel, followed by the period over which the plug is pulled through the probe setup. The peak of the plug goes off of the plot, but entire plug alkalinity profiles for each 75% initial DIC-to-alkalinity ratio condition, for 1, 5, 10, and 15 minute duration adsorption CV steps, can be seen in the left pane of Figure 24. The right pane of Figure 24 shows the plug alkalinity profiles for the 1, 10, and 15 minute duration adsorption CV step experiments at a 99% initial DIC-to-alkalinity ratio.

From the plug alkalinity profiles, we see that the maximum of the profiles vary for different duration adsorption CV steps. We can observe this variation more clearly in the left pane of Figure 25, where we have plotted a point for the maximum point of the plug alkalinity profile for each experiment conducted. We see that, while the 15 minute condition was lower than the 10 minute condition for both 75% and 99% initial DIC experiments, the 1 minute condition was higher than both for 75% and lower than both for 99%. And for the 75% conditions, the 5 minute condition was the highest. This suggests there was an optimal duration for binding alkalinity that varies as a function of the initial DIC-to-alkalinity ratio, but not monotonically as we might expect, with a longer adsorption time resulting in more bound alkalinity that could be desorbed.

In Figures 26 and 27, we show more detailed plots of how the values of alkalinity and DIC in the plug vary for 75% and 99% initial DIC conditions, respectively. Here, to observe the drop off in the concentration of each for larger plug volumes, the average alkalinity and DIC have been calculated for the peak 3.5 mL, peak 7 mL, and entire 14 mL of each plug. In the upper-right pane for each, we can easily read off the concentration factor for each experiment and each plug volume. We see that the maximum concentration factor for each initial 75% DIC experiment is roughly 4, dropping to roughly 2 for the 14 mL plug volumes. For the initial 99% DIC experiments, the concentration factors are somewhat lower for each respective plug volume, ranging from roughly 3 at the maximum to between 1.5 and 2 for the 14 mL plug volumes

In the lower left-hand pane for each of 26 and 27, we see that plug DIC-to-alkalinity ratio decreased for larger plug volumes for every experiment in both 75% and 99% conditions. Moreover, the plug DIC-to-alkalinity was significantly lower than the feed DIC-to-alkalinity values for both 75% and 99% conditions. While this lower plug DIC-to-alkalinity ratio was roughly consistent for each adsorption CV duration at 75%, it varied significantly at 99%. For both, we see that there was a decrease in the plug DIC-to-alkalinity ratio as the adsorption CV duration increased.
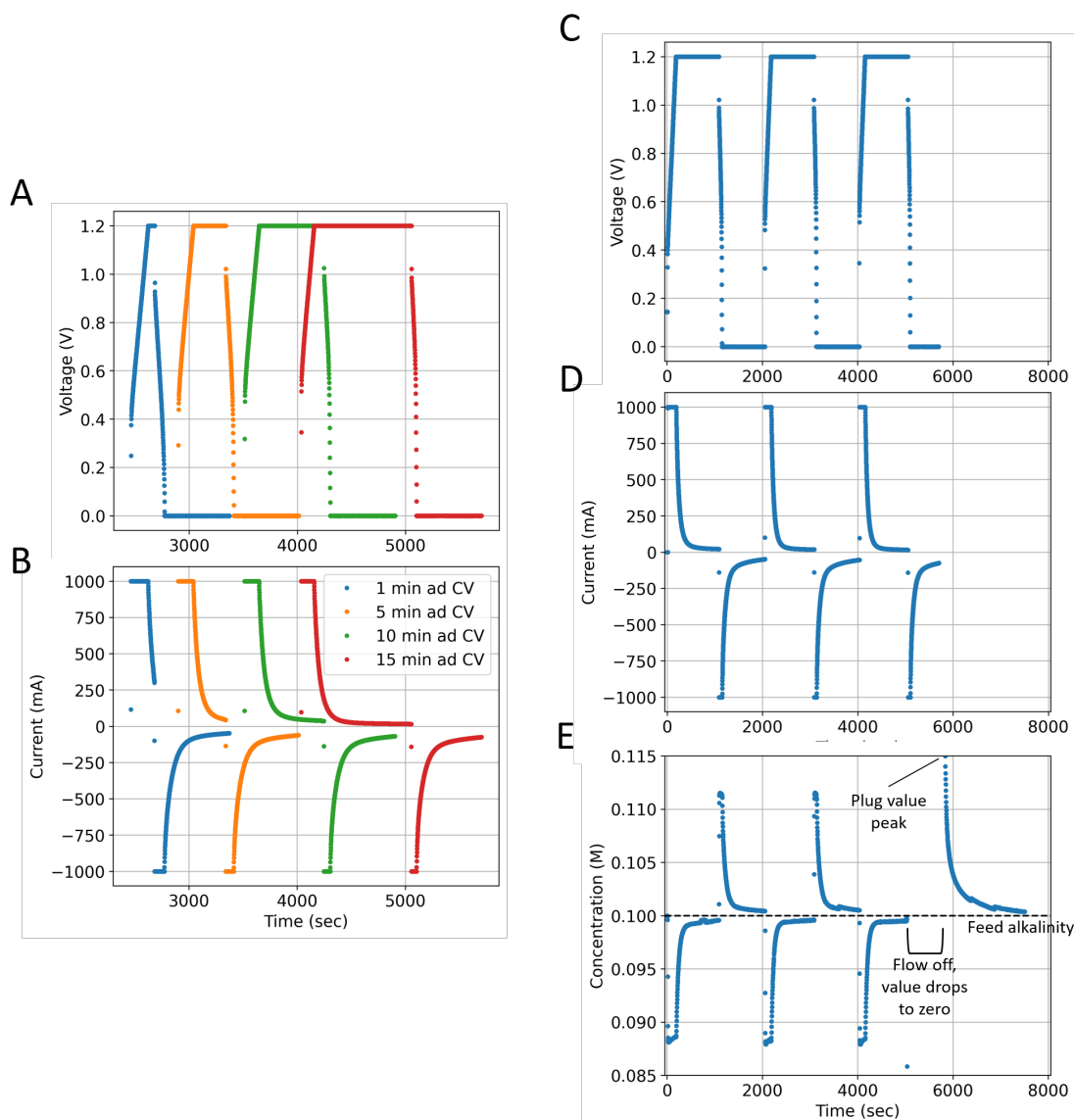
Figure 23: **Raw data for 75% initial DIC-to-alkalinity ratio conditions. A** Voltage for entire second cycle, adsorption half-cycle followed by desorption half-cycle, for experiments with 1, 5, 10, and 15 minute adsorption CV steps. **B** Current for same series of experiments. **C-E** Voltage, current, and alkalinity for all three cycles and the post-cycle desorption for the 15 minute adsorption CV step experiment.

This decrease is consistent with the exchange of carbonate for bicarbonate that we expect from the Donnan potential if bicarbonate and carbonate ions were initially bound by the electrode roughly in proportion to their solution concentration. As the adsorption step continues, the exchange of carbonate for pairs of bicarbonate in the electrode reduces the quantity of DIC bound on the electrode. After adsorption, there is less DIC that can desorb into the plug. We expect to see a more pronounced drop off in the DIC-to-alkalinity ratio for the 99% condition because, initially, given that the feed is almost entirely bicarbonate, almost all of the bound ions on the electrode will also be bicarbonate.

In Figure 28, we plot the solution partial pressure of CO_2 for each duration experiments for 75% and 99% initial DIC conditions. For an ideal ACS cycle, in which there is no exchange of carbonate for bicarbonate on the electrode, the post-concentration p_{CO_2} will always increase, as long as the concentration factor is greater than 1. In these experiments, however, we see that the p_{CO_2} almost always decreased. But this is not surprising given that the
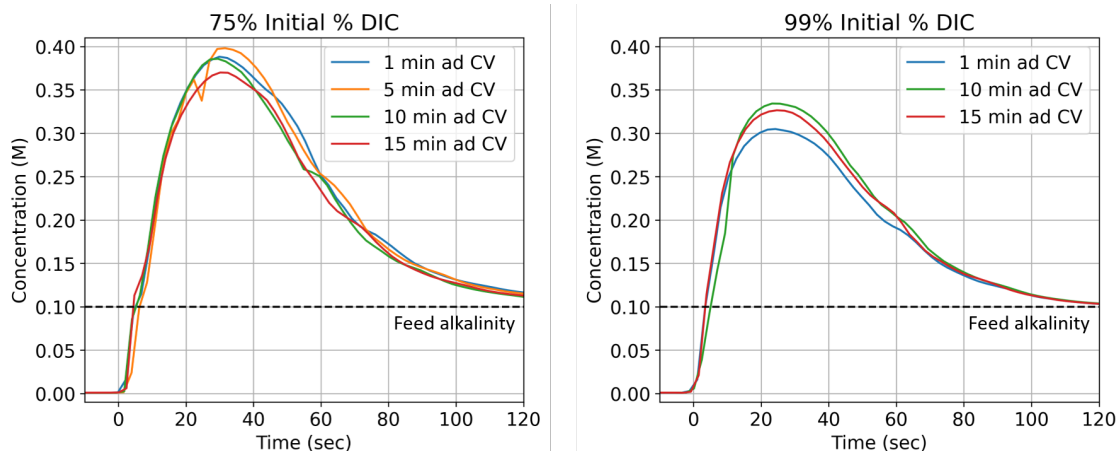
27

Figure 24: **Plug alkalinity profiles for each duration adsorption CV step experiments**, at a 75% initial DIC-to-alkalinity ratio (left) and at a 99% initial DIC-to-alkalinity ratio (right).
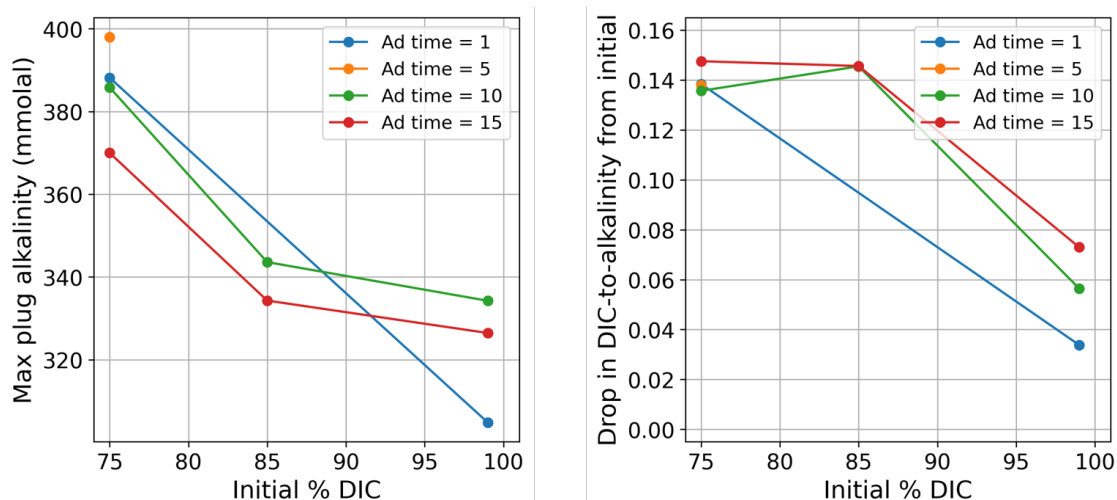

Figure 25: **Initial % DIC vs maximum plug alkalinity and drop in DIC-to-alkalinity ratio.**

plug DIC-to-alkalinity decreased — the lower quantity of DIC, and in particular lower quantity of bicarbonate, that was desorbed into the plug meant that the plug had less DIC to up-concentrate and, ultimately, a lower p_{CO_2}, even after concentration. We can conclude that, for the level of carbonate exchange for bicarbonate that occurred in most conditions, the exchange was able to more than compensate for the concentration of the solution, suppressing the ACS.

The exceptions are the 1 and 10 minute duration adsorption CV step experiments for the 99% initial DIC, seen in the right pane in Figure 28. We see that, for the 1 minute condition, both the 3.5 and 7 mL peak volumes had a higher p_{CO_2} than the feed, while, for the 10 minute condition, only the maximum plug concentration had a higher p_{CO_2} than the feed. In these experiments, the ACS did result in an increase in the p_{CO_2}, even if it was significantly lower than it would have been had there been no carbonate exchange for bicarbonate.

In Figure 29, we plot the C_{out} values, in solid lines, that we would obtain from each volume of the concentrated plug if it had been exposed to a vacuum with CO_2 partial pressure of $p_{out} = 50$ mbar. We see that, despite having an increased p_{CO_2} (Figure 28), these two conditions would not have resulted in a positive quantity of CO_2 being outgassed because, along with all of the other conditions, none of the plug volumes had a $p_{CO_2} > 50$ mbar. The only portion of a plug that exceeded 50 mbar in Figure 28 was the maximum point of the 1 minute duration 99% plug.
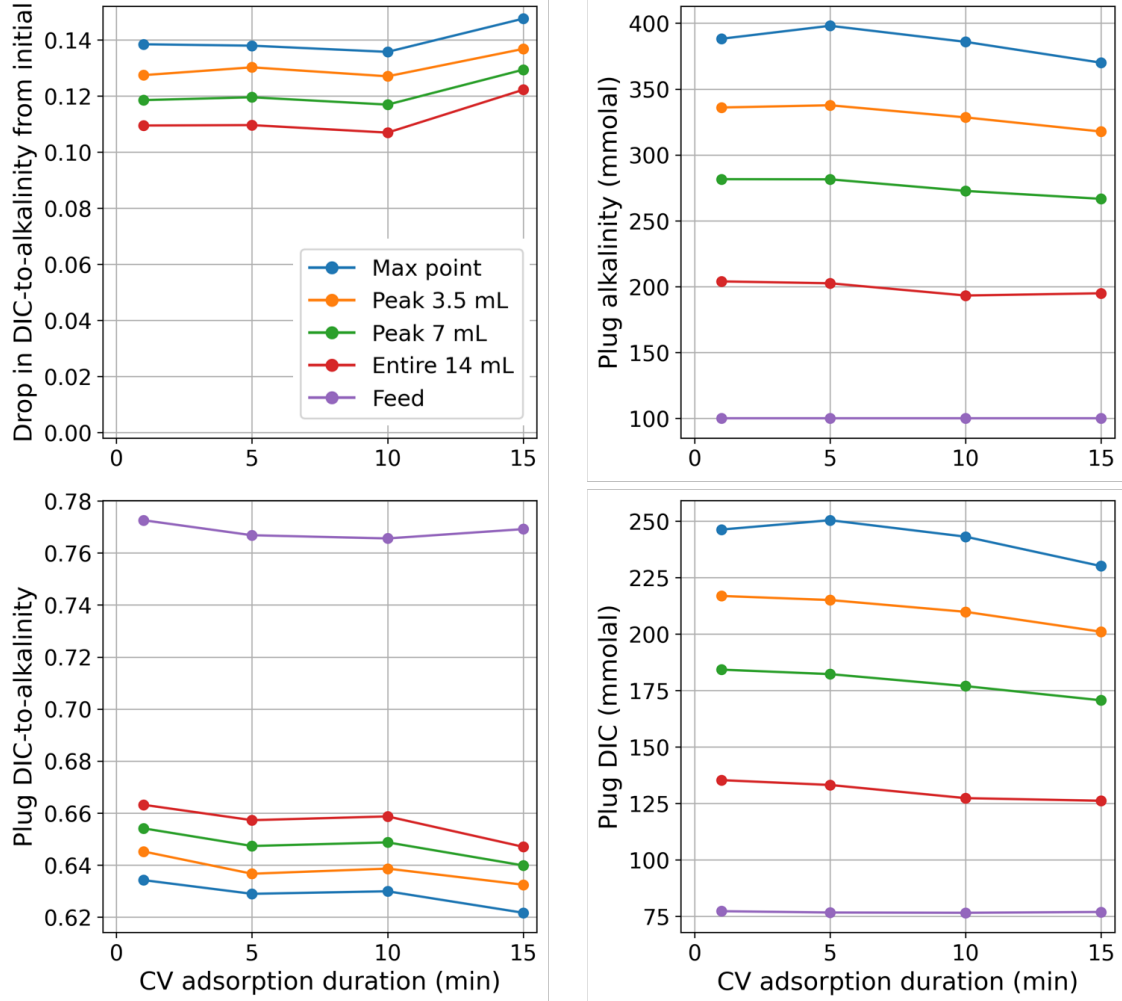
28

Figure 26: **Varying plug volumes for varying duration adsorption CV steps, 75% DIC.**

We also plotted, in dashed lines in Figure 29, the hypothetical C_{out} values we would have obtained had there not been a drop in the DIC-to-alkalinity ratio between the feed and the plug volumes. The purpose here is to simulate what we would expect if CDI did not underperform expectations due to the exchange of carbonate for bicarbonate on the electrode. We see that, for the 75% initial DIC experiments, while the p_{CO_2} would have gone up and resulted in a higher C_{out} value, it still would have been negative. A 75% initial DIC is simply too low to be able to obtain CO_2 outgassing when the concentration factor is only roughly 4. For the 99% initial DIC experiments, however, a fixed DIC ratio would have results in a positive C_{out} value for each duration adsorption CV step and each plug volume. Moreover, the value of C_{out} would have been roughly constant for increasing adsorption CV step duration, indicating that a shorter duration would not have significantly suppressed the ACS.

Finally, in Figure 30, we plot the C_{out} values for the 3.5 mL plug volume for p_{out} = 50 mbar and, in a dashed line, the hypothetical C_{out} values if the 3.5 mL plug volumes had been up-concentrated by another factor of four, and then exposed to a p_{out} = 50 mbar. For these conditions, the 3.5 mL plug volume alkalinities were between 250 and 300 mmolal, so another factor of four would corresponds to a final alkalinity of between 1.0 and 1.2 molal. This is consistent with the maximum plug values that Porada *et al.* estimate for cells very similar to the one used for these experiments.[32]
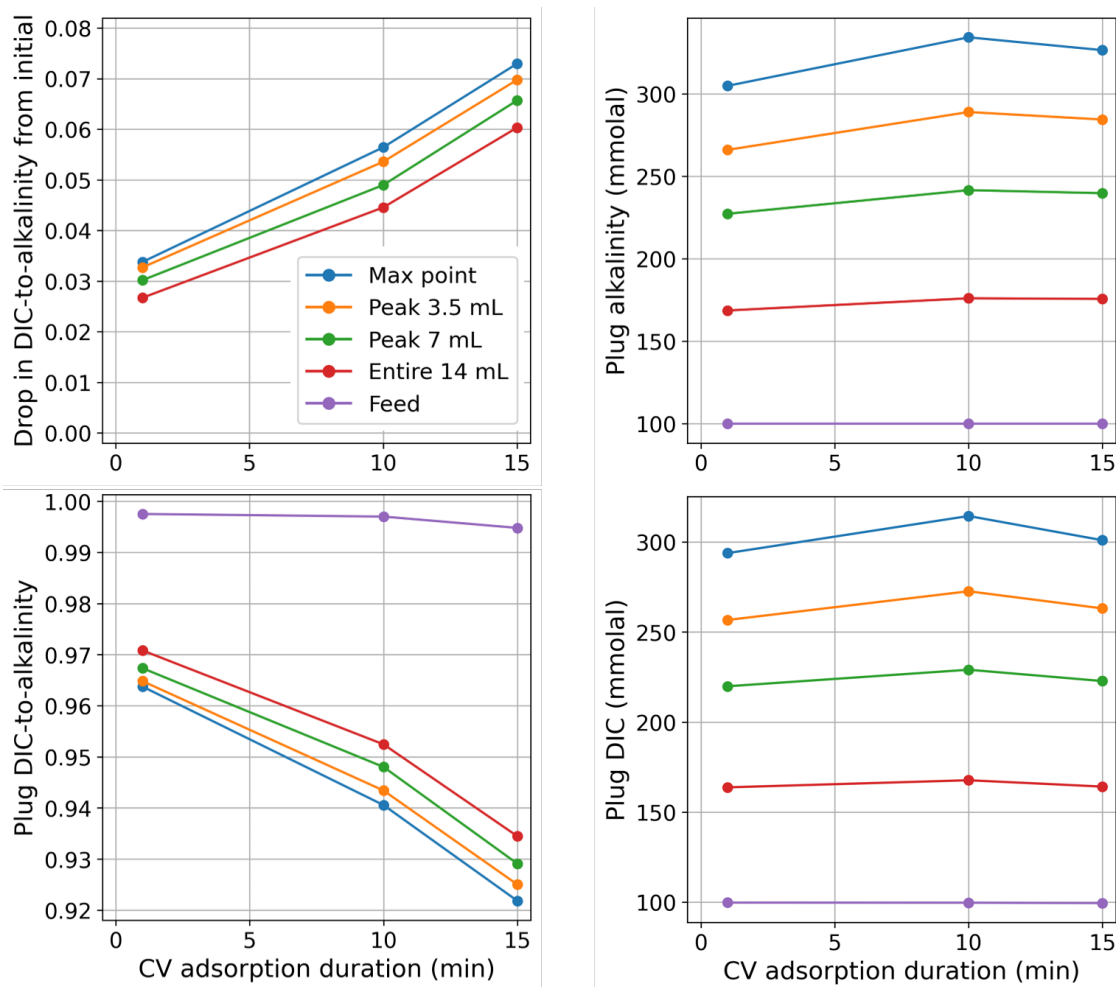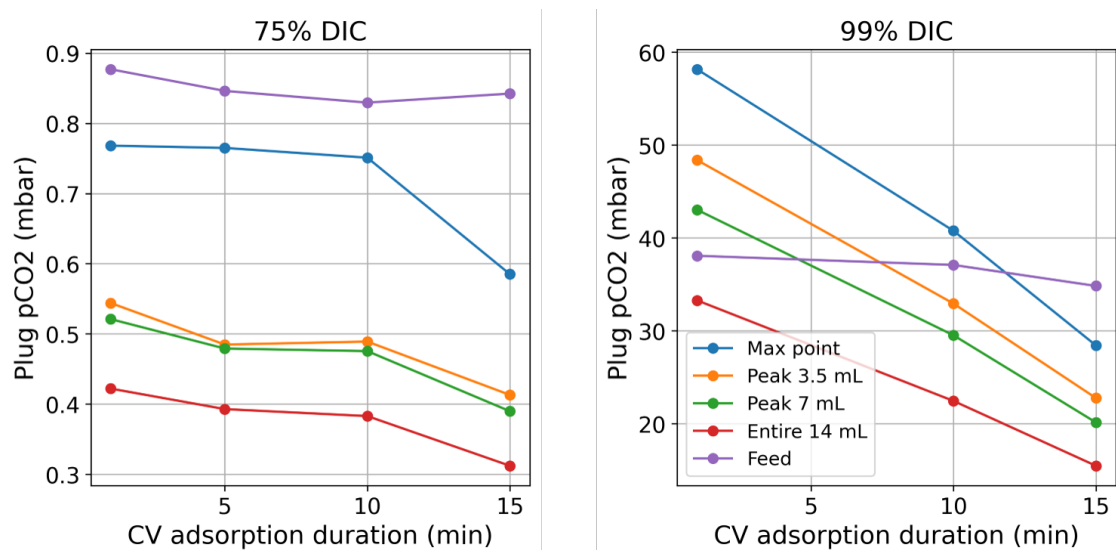
Figure 27: **Varying plug volumes for varying duration adsorption CV steps, 99% DIC.**

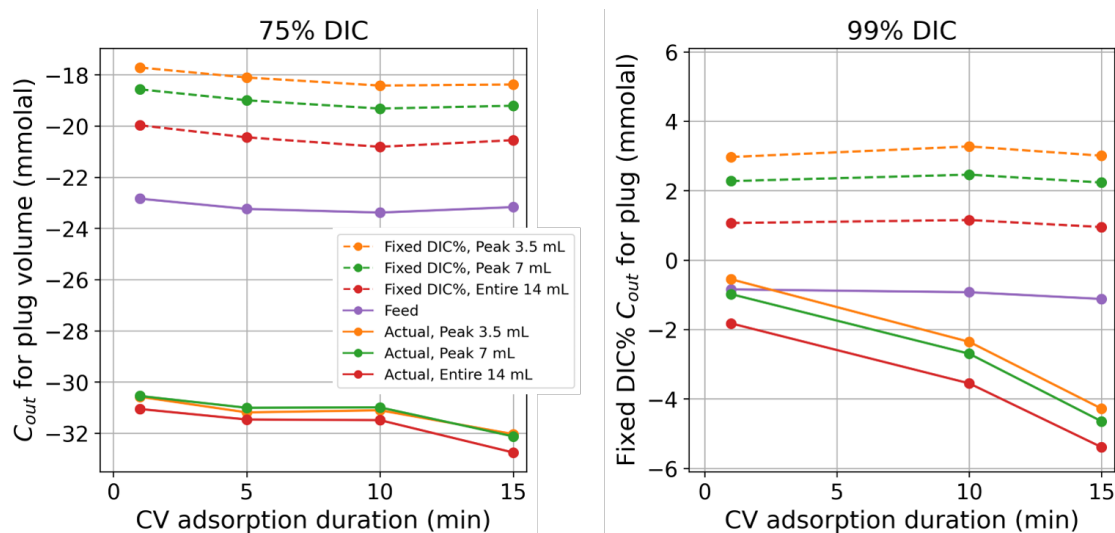Figure 28: **Plug solution pCO$_2$ vs adsorption CV duration, for varying plug volumes, 75% DIC.**

Figure 29: **Plug C_{out} vs adsorption CV duration for p_{out} = 50 mbar, for varying plug volumes.** Solid lines represent the actual values; dashed lines are hypothetical if the DIC % had been fixed.
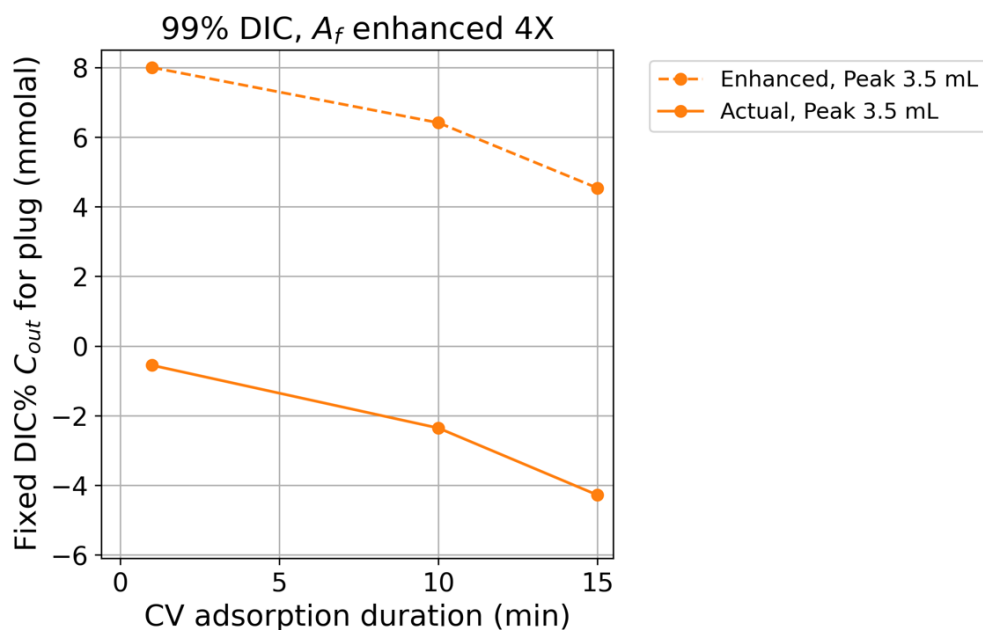

Figure 30: **Plug C_{out} vs adsorption CV duration for p_{out} = 50 mbar.** Solid line is based on the actual concentration factor; dashed line is hypothetical based on an enhanced concentration factor of an additional factor of 4.

7.4 Implications

Because of the exchange between carbonate ions and pairs of bicarbonate ions, the ACS is suppressed for MCDI at an initial alkalinity of 100 mmolal, even at a high initial DIC-to-alkalinity of 99%. In these experiments, bicarbonate ions initially bound by the electrode were expelled back into the flow channel, and discarded, in exchange for carbonate ions. If we had retained and concentrated the bicarbonate-rich by-product that we discarded, however, and the carbonate-rich or bicarbonate-poor solution being concentrated was discarded, we could have enhanced the ACS. This ability to select for a bicarbonate-rich solution and enhance the solution DIC-to-alkalinity ratio is explored in the next section.

We observed that C_{out} would have been roughly constant for increasing adsorption CV step duration for the 99% initial DIC conditions (Figure 29), indicating that a shorter duration would not have significantly suppressed the ACS. We can conclude that, if we were to use MCDI electrodes that did not select for carbonate ions over bicarbonate ions, we would be able to outgas CO_2 even for short duration adsorption steps. Guyes *et al.* have implemented monovalent selective electrodes for cationic systems by chemically functionalizing and adding charge to the electrode.[?]

To implement an effective MCDI-driven concentration module, we would also need to obtain higher concentration factors. Early-stage experimental and modeling results with our collaborator, Slawomir Porada, indicate that it should be possible to increase the concentrated plug alkalinity to above 1.5 molal, and potentially higher, by adding thicker electrodes without changing the volume of the flow channel. The current architecture of MCDI cells is optimized for desalination, which does not benefit from generating a highly concentrated solution stream, so there are likely still unexplored ways to optimize an MCDI cell for use as an ACS selection module.

8 The need for bicarbonate-enrichment to integrate the ACS cycle

The core property of the alkalinity concentration swing is that increasing the concentration of a DIC-loaded alkaline solution increases the solution partial pressure of CO_2. However, without modification, the ACS cycle faces significant shortcomings making it an infeasible direct air capture approach.

In particular, the initial ACS analysis is based on an important limitation: the input and output CO_2 partial pressures for the cycle were both set to 0.4 mbar, or atmospheric CO_2 levels. While this allows for understanding the limiting thermodynamic properties of the cycle, it does not correspond to a practical engineering condition. Reaching these conditions would require outgassing pressures that are below the vapor pressure of water.

Applying cycle parameters farther from atmospheric equilibrium conditions, such as $p_{in} = 0.3$ mbar and $p_{out} = 50$ mbar, allows for a more realistic process assessment. However, at these conditions, the unmodified ACS has very limited operating conditions that result in removed CO_2. Initial alkalinity would have to be extremely low, close to 10 mM, and final alkalinity very high, above 2 M. The result is a very low cycle capacity (<1 mM), and very slow absorption timescales, even if energy costs are still within a reasonable range.

For this reason, we explored the possibility of enhancing the ACS through an approach called the bicarbonate-enriched alkalinity concentration swing (BE-ACS). Based on the realization that bicarbonate ions are the active species that result in CO_2 outgassing through disproportionation, we developed a model to consider a bicarbonate-carbonate selectivity module. Processing the feed solution to create a bicarbonate-rich stream allows us to overcome the shortcomings described here and to improve the three key figures of merit: cycle capacity, absorption rate, and specific work.

8.1 Bicarbonate-enrichment principle

Throughout this work we have drawn attention to the importance of controlling the DIC-to-alkalinity ratio of a solution. Whereas absorption conditions for alkaline solutions are at low DIC-to-alkalinity ratios (close to 0.5, where carbonate ions dominate), outgassing requires high DIC-to-alkalinity ratio (close to 1, where bicarbonate ions dominate). As depicted in Figure 31, we can obtain a high C_{out} and high solution partial pressure with only modest concentration factors, comparable to those we've demonstrated in this work, if we can enrich the bicarbonate concentration in solution, and thereby increase the DIC-to-alkalinity ratio. Adding a bicarbonate-carbonate selection step represents a modification of the initially-proposed ACS process. This modified process is called the bicarbonate-enriched alkalinity concentration swing. As demonstrated in the following section, we were able to achieve such a selection step by using CDI to implement this process.
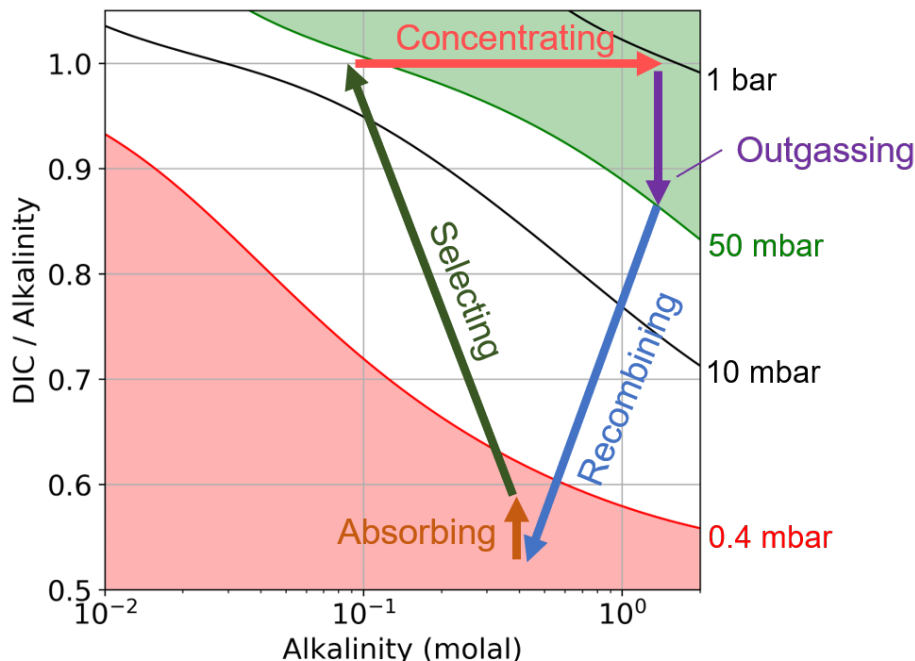
Figure 31: **Bicarbonate-enriched alkalinity concentration swing.** This diagram depicts the five steps of the BE-ACS cycle in DIC-to-alkalinity and alkalinity space. The solution CO_2 partial pressure contour lines are plotted. The red region represents a solution below 0.4 mbar (or roughly atmospheric partial pressure). And the green region represents a reasonable vacuum outgassing target, slightly above the vapor pressure of water at ambient conditions. The arrows depict a direct air capture cycle moving the system from absorption (orange arrow) to outgassing (purple arrow), by using CDI for bicarbonate-carbonate selection (green arrow) and reverse osmosis for concentration (red arrow).

8.2 Using CDI for bicarbonate enrichment

Figure 32 plots experimental results from the capacitive deionization cell demonstrating that MCDI can be used to increase the DIC-to-alkalinity ratio of a solution. This is driven by preferential binding of carbonate and hydroxide ions on the electrode, which increases the relative ratio of bicarbonate ions (and thereby increases the DIC-to-alkalinity ratio). Electrode binding properties are not discussed in detail in this study, but are the subject of forthcoming publications. This effect holds across a range of initial DIC-to-alkalinity ratios. The results in Figure 32 indicate that, for the MCDI cell used, a two-stage selection protocol can be used to enrich a solution beginning below ambient CO_2 partial pressure to a nearly 100% bicarbonate solution: the first step begins at 130 mmolal alkalinity below ambient CO_2 partial pressure (the right most green square) and the second step begins at roughly 100 mmolal alkalinity (the right most blue square).

9 Integrating the bicarbonate-enriched ACS

After independently testing each of the components of the BE-ACS approach, 1) bicarbonate-enrichment; 2) concentration of an alkaline solution; 3) CO_2 extraction; and 4) dilution and re-equilibration with air, we were able to demonstrate the full BE-ACS cycle.

Figure 33 reports three conditions, tested at 50 mM and 150 mM of alkalinity, and at 92% and 100% DIC-to-alkalinity ratio. Each condition corresponds to the state after the CDI bicarbonate-enrichment module but before the RO concentration step. The reported energy values in kJ/mol of CO_2 are significantly higher than desired DAC processes. However, at this stage of first lab-scale experiment, this work focused on demonstrating a proof of principle effect, rather than driving down the energy cost or optimizing process conditions. The table reports the amount of outgassed
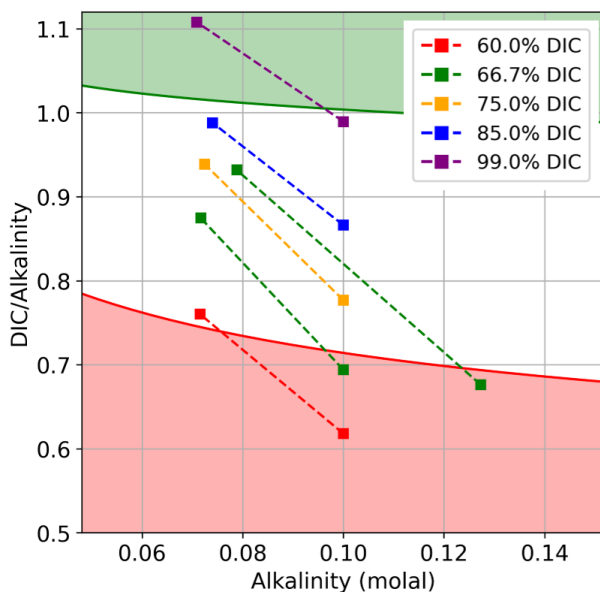
Figure 32: **CDI selectivity.** Experimental data using the CDI cell to increase the DIC-to-alkalinity ratio of a given solution. Starting conditions are at the bottom right of each dashed line, and post-selection conditions are at the top left. Each color corresponds to a different starting condition with a different DIC-to-alkalinity ratio. Moving up in the DIC-to-alkalinity ratio raises the ratio of bicarbonate to carbonate concentrations in the solution.

CO_2 per cycle. The penultimate column, shaded in orange, represents lower energy costs if a multi-stage RO process is achieved. The final column reports the energy requirements if the concentration and extraction process are operating at the thermodynamic limit, at the same extracted CO_2 quantity.

The multi-stage model and the thermodynamic minimum calculation are described in detail in Section 4, "ACS thermodynamics and energy models," of our previous work.[6] The multi-stage model is based on the Van't Hoff assumption that the osmotic pressure is proportional to the difference in salt concentration across the membrane. Each stage concentrates the solution by a factor of two, until the desired concentration factor is reached.

Alk. (M)	DIC (M)	Alk. (M)	Conc. factor	C_{out} (mmoles)	E_{CO_2} Exp. (kJ/mol)	E_{CO_2} Multi-stage (kJ/mol)	E_{CO_2} Thermo. min (kJ/mol)
0.05	0.05	0.365	**7.3x**	**0.0828**	**5100**	1100	730
0.15	0.138	0.968	**6.5x**	**0.234**	**2600**	1000	700
0.15	0.149	0.926	**6.2x**	**0.682**	**900**	360	250

Feed condition	Experimental measurement	Theoretical energy model analysis

Figure 33: **Experimental quantification of energy cost.** Three conditions were tested at 50 mM and 150 mM of alkalinity, and at 92% and 100% DIC-to-alkalinity ratio. Each line corresponds to the state after exiting the CDI bicarbonate-enrichment module, but before the RO concentration step.

Using the energy models developed in Rinberg et al. (2021), we were able to study how operating conditions affect BE-ACS performance to test how much further the molar work requirement could decrease upon optimization of the BE-ACS process. We take the initial alkalinity and DIC concentration as in Figure 33 and study the C_{out} and

34

energy values if each condition is concentrated up to 1 molal of alkalinity. Using these conditions, Figure 34 reports the theoretical energy and cycle capacity for a system that recovers CO_2 from the both the permeate stream and the concentrate stream. Multi-stage reverse osmosis energy modelling is used to estimate the capture energy using the methodology that we previously reported.[6] We also include the thermodynamic minimum work values for reference. The significant improvement in capture energy suggests that there is substantial improvement that can be achieved beyond the initial proof of principle demonstration reported in this work.

Alk. (M)	DIC (M)	Alk. (M)	Conc. Factor	C_{out} (mmoles)	E_{CO2} Exp. (kJ/mol)	E_{CO2} Multi-stage (kJ/mol)	E_{CO2} Thermo. min (kJ/mol)
0.05	0.05	1	**20x**	**1.11**	**1000**	160	110
0.15	0.138	1	**6.6x**	**8.51**	**590**	230	160
0.15	0.149	1	**6.6x**	**5.68**	**240**	100	70

Feed condition   Modelled based on feed conditions   Theoretical energy model analysis

Figure 34: **Modelled quantification of energy cost.**

References

[1] IPCC. *Global warming of 1.5°C*. January 2018.

[2] Valérie Masson-Delmotte, Panmao Zhai, Anna Pirani, Sarah L. Connors, Clotilde Péan, Sophie Berger, Nada Caud, Yang Chen, Leah Goldfarb, Melissa I. Gomis, Mengtian Huang, Katherine Leitzell, Elisabeth Lonnoy, J. B. Robin Matthews, Thomas K. Maycock, Tim Waterfield, Özge Yelekçi, Rong Yu, and Botao Zhou, editors. *Climate Change 2021: The Physical Science Basis. Contribution of Working Group I to the Sixth Assessment Report of the Intergovernmental Panel on Climate Change*. Cambridge University Press, Cambridge, United Kingdom and New York, NY, USA, 2021.

[3] Andrew Bergman and Anatoly Rinberg. The Case for Carbon Dioxide Removal: From Science to Justice. In *CDR Primer*. edited by J. Wilcox, B. Kolosz, J. Freeman, January 2021. https://cdrprimer.org/read/chapter-1.

[4] Dominic Lenzi. The ethics of negative emissions. *Global Sustainability*, 1(E7), 2018.

[5] K. Anderson and G. Peters. The trouble with negative emissions. *Science*, 354(6309):182–183, October 2016.

[6] Anatoly Rinberg, Andrew M. Bergman, Daniel P. Schrag, and Michael J. Aziz. Alkalinity Concentration Swing for Direct Air Capture of Carbon Dioxide. *ChemSusChem*, 14(20):4439–4453, 2021. _eprint: https://onlinelibrary.wiley.com/doi/pdf/10.1002/cssc.202100786.

[7] David L. Parkhurst and C.A.J. Appelo. Description of input and examples for PHREEQC version 3: a computer program for speciation, batch-reaction, one-dimensional transport, and inverse geochemical calculations. USGS Numbered Series 6-A43, U.S. Geological Survey, Reston, VA, 2013.

[8] Xiaoguang Wang, William Conway, Robert Burns, Nichola McCann, and Marcel Maeder. Comprehensive Study of the Hydration and Dehydration Reactions of Carbon Dioxide in Aqueous Solution, December 2009. Archive Location: world Publisher: American Chemical Society.

[9] P. V. Danckwerts. Absorption by simultaneous diffusion and chemical reaction. *Transactions of the Faraday Society*, 46(0):300–304, January 1950. Publisher: The Royal Society of Chemistry.

[10] P. V. Danckwerts and A. M. Kennedy. The kinetics of absorption of carbon dioxide into neutral and alkaline solutions. *Chemical Engineering Science*, 8(3):201–215, June 1958.

[11] David W. Keith, Geoffrey Holmes, David St. Angelo, and Kenton Heidel. A Process for Capturing CO2 from the Atmosphere. *Joule*, 2(8):1573–1594, August 2018.

[12] Joshuah K. Stolaroff, David W. Keith, and Gregory V. Lowry. Carbon Dioxide Capture from Atmospheric Air Using Sodium Hydroxide Spray. *Environmental Science & Technology*, 42(8):2728–2735, April 2008.

[13] S. S. Laddha and P. V. Danckwerts. Reaction of CO2 with ethanolamines: kinetics from gas-absorption. *Chemical Engineering Science*, 36(3):479–482, January 1981.

[14] Ujjal K. Ghosh, Sandra E. Kentish, and Geoff W. Stevens. Absorption of carbon dioxide into aqueous potassium carbonate promoted by boric acid. *Energy Procedia*, 1(1):1075–1081, February 2009.

[15] Ayanne de Oliveira Maciel, Paul Christakopoulos, Ulrika Rova, and Io Antonopoulou. Carbonic anhydrase to boost CO2 sequestration: Improving carbon capture utilization and storage (CCUS). *Chemosphere*, 299:134419, July 2022.

[16] Sefli Sri Wahyu Effendi and I-Son Ng. The prospective and potential of carbonic anhydrase for carbon dioxide sequestration: A critical review. *Process Biochemistry*, 87:55–65, December 2019.

[17] Sonja Salmon and Alan House. Chapter 2 - Enzyme-catalyzed Solvents for CO2 Separation. In Fan Shi and Bryan Morreale, editors, *Novel Materials for Carbon Dioxide Mitigation Technology*, pages 23–86. Elsevier, Amsterdam, January 2015.

[18] P. C. Tseng, W. S. Ho, and D. W. Savage. Carbon dioxide absorption into promoted carbonate solutions. *AIChE Journal*, 34(6):922–931, 1988. _eprint: https://onlinelibrary.wiley.com/doi/pdf/10.1002/aic.690340604.

[19] Tohid Nejad Ghaffar Borhani, Abbas Azarpour, Vahid Akbari, Sharifah Rafidah Wan Alwi, and Zainuddin Abdul Manan. CO2 capture with potassium carbonate solutions: A state-of-the-art review. *International Journal of Greenhouse Gas Control*, 41:142–162, October 2015.

[20] Edward Jones, Manzoor Qadir, Michelle T. H. van Vliet, Vladimir Smakhtin, and Seong-mu Kang. The state of desalination and brine production: A global outlook. *Science of The Total Environment*, 657:1343–1356, March 2019.

[21] Menachem Elimelech and William A. Phillip. The Future of Seawater Desalination: Energy, Technology, and the Environment. *Science*, 333(6043):712–717, August 2011.

[22] Anthony P. Straub, Akshay Deshmukh, and Menachem Elimelech. Pressure-retarded osmosis for power generation from salinity gradients: is it viable? *Energy & Environmental Science*, 9(1):31–48, January 2016.

[23] Ying Mei and Chuyang Y. Tang. Recent developments and future perspectives of reverse electrodialysis technology: A review. *Desalination*, 425:156–174, January 2018.

[24] Ramato Ashu Tufa, Sylwin Pawlowski, Joost Veerman, Karel Bouzek, Enrica Fontananova, Gianluca di Profio, Svetlozar Velizarov, João Goulão Crespo, Kitty Nijmeijer, and Efrem Curcio. Progress and prospects in reverse electrodialysis for salinity gradient energy conversion and storage. *Applied Energy*, 225:290–331, September 2018.

[25] Effect of Different Draw Solutions on Concentration Polarization in a Forward Osmosis Process: Theoretical Modeling and Experimental Validation | Industrial & Engineering Chemistry Research.

[26] M.J. Francis and R.M. Pashley. The effects of feed water temperature and dissolved gases on permeate flow rate and permeate conductivity in a pilot scale reverse osmosis desalination unit. *Desalination and Water Treatment*, 36(1-3):363–373, December 2011. Publisher: Taylor & Francis _eprint: https://doi.org/10.5004/dwt.2011.2511.

[27] S. Porada, R. Zhao, A. van der Wal, V. Presser, and P. M. Biesheuvel. Review on the science and technology of water desalination by capacitive deionization. *Progress in Materials Science*, 58(8):1388–1442, October 2013.

[28] M. E. Suss, S. Porada, X. Sun, P. M. Biesheuvel, J. Yoon, and V. Presser. Water desalination via capacitive deionization: what is it and what can we expect from it? *Energy & Environmental Science*, 8(8):2296–2319, July 2015.

[29] J. G. Gamaethiralalage, K. Singh, S. Sahin, J. Yoon, M. Elimelech, M. E. Suss, P. Liang, P. M. Biesheuvel, R. L. Zornitta, and L. C. P. M. De Smet. Recent advances in ion selectivity with capacitive deionization. *Energy & Environmental Science*, 14(3):1095–1120, 2021.

[30] P. M. Biesheuvel, H. V. M. Hamelers, and M. E. Suss. Theory of Water Desalination by Porous Electrodes with Immobile Chemical Charge. *Colloids and Interface Science Communications*, 9:1–5, November 2015.

[31] T. M. Mubita, J. E. Dykstra, P. M. Biesheuvel, A. van der Wal, and S. Porada. Selective adsorption of nitrate over chloride in microporous carbons. *Water Research*, 164:114885, November 2019.

[32] S. Porada, Li Zhang, and J. E. Dykstra. Energy consumption in membrane capacitive deionization and comparison with reverse osmosis. *Desalination*, 488:114383, August 2020.